Combustion chamber design for a high-performance natural gas engine: CFD modeling and experimental investigation

Combustion chamber design for a high-performance natural gas engine: CFD modeling and experimental investigation

Mirko Baratta, Daniela Misul, Ludovico Viglione, Jiajie Xu

Dipartimento Energia, Politecnico di Torino – Torino, Italy

ABSTRACT

The present paper is focused on the development of a high-performance, monofuel, spark ignition engine running on natural gas, featuring a high volumetric compression ratio and a variable valve actuation system. More specifically, the cylinder head geometry effect has been analyzed and the compression ratio has been optimized by means of steady-state and transient simulation activity, as well as of an extensive experimental campaign. The compression ratio effect was mainly investigated by means of experimental tests but a few 3D simulations were also run in order to quantify its impact on the in-cylinder tumble and turbulence. The main novelty of the paper are, first, the adoption of very high engine compression ratio values, second, the combined optimization of the cylinder head design and compression ratio. The main results can be summarized as follows. The engine configuration with mask showed a decrease in the average discharge coefficient by 20-30% and an increase in the tumble ratio by around 200% at partial load. Moreover, the simulation of the engine cycle indicated that the presence of the piston modifies the tumble structure with respect to the steady-state simulation case. An increase in the tumble number and turbulence intensity by around 90% and 10%, respectively, are obtained for the case with mask at 2000 rpm and 4 bar. With reference to the combustion duration, on an average, the presence of the masking surface led to a reduction of the combustion duration (from 1% to 50% of mass fraction burned) between 2 and 6 degrees. As far as the engine compression ratio is concerned, the value of 13 was finally selected as

the best compromise between combustion variability, engine performance at full load and fuel consumption at partial load.

KEYWORDS

Natural gas, SI engines, Tumble flow, CFD simulation.

NOMENCLATURE

B	cylinder bore
bmep	brake mean effective pressure
CA	crank angle
C_D	discharge coefficient
CFD	computational fluid dynamics
CNG	compressed natural gas
CoV	coefficient of variation
CR	compression ratio
deg	degree
ECFM	extended coherent flamelet model
EGR	exhaust gas recirculation
GHG	greenhouse gases
imep	indicated mean effective pressure
k	turbulent kinetic energy
MBT	maximum brake torque
MFB	mass-fraction burned
MFB1-50	combustion duration from 1% to 50% of heat released

MFB50	‘combustion barycenter’ position
NG	natural gas
N_T	tumble number
PFP	peak firing pressure
PMAX0	ensemble-averaged peak firing pressure
PMAXmx	maximum cycle-resolved peak firing pressure
SI	spark ignition
TN	in-cylinder tumble number
TR	tumbling ratio
v_{is}	isentropic flow velocity
VVA	variable valve actuation
x	coordinate for tumble moment of momentum calculation
y+	normalized distance from wall

Greek symbols

ε	turbulence dissipation rate
θ	crank angle position
$\omega_{AV,EXH}$	equivalent angular speed to the exhaust side
$\omega_{AV,INT}$	equivalent angular speed to the intake side

1. INTRODUCTION

Nowadays, the design of modern internal combustion (IC) engines represents a challenging task, due to the raising concern for the global warming as well as to the stringent constraints set by the current pollutant regulations. The use of gasoline or diesel in internal combustion engines is likely to remain the most cost-effective overall ground-based transportation propulsion system for the near future. Furthermore, hybrid and electric vehicles are gaining considerable market share. However, as far as IC engines are concerned,

natural gas (NG) represents a factual alternative to traditional fuels thanks to the reduced pollutant and carbon dioxide emissions [1,2]. Moreover, the development of engines compatible with biofuels (for example, natural gas from biomasses) can provide enormous benefits compared to fossil fuels, in terms of greenhouse gases (GHG) emissions [3,4], although attention has to be paid to the fuel properties and their dependence on the blend composition. With specific reference to natural gas, the effect of biogas composition on the engine operating characteristics has been widely studied by the researchers. In [5] it was found that methane concentration in the biogas significantly improves performance and reduces emissions of hydrocarbons. The lean operation limit is also extended. Similarly, investigations carried out in [6] showed that the methane-enriched biogas performed similarly to compressed natural gas (CNG). Along with methane, other inert species, such as carbon dioxide and nitrogen, can be present in the biogas composition. Furthermore, hydrogen derived from biomass gasification can be blended to natural gas as an additive. As a matter of fact the high speed of flame propagation of hydrogen improves the stability of the combustion process when added to natural gas [7,8].

The development of highly efficient engines cannot withstand the adoption of advanced design methods. As a matter of fact, the introduction of advanced engine concepts, such as, variable valve actuation, turbocharging or direct injection leads to an increase in the complexity of the engine design process, as the number of the design variables is remarkably higher. Moreover, with reference to biofuels dedicated control algorithms might be necessary to make up for the variability in the fuel properties due to the dispersion in the blend composition. As far as the optimization of the combustion chamber and the intake port geometry is concerned, the adoption of computational fluid dynamics (CFD) represents an effective means to support the design process, allowing the time and cost of the associated experimental activity to be reduced. Appreciable benefits in terms of combustion stability, efficiency and pollutant emissions can be obtained if a suitable intensity of swirl and/or tumble motion is targeted. With specific reference to spark ignition (SI) engines, the tumble motion is usually generated in order to increase the turbulence level in the combustion chamber, thus enhancing the combustion stability and the exhaust gas recirculation (EGR) tolerance. Amer and Reddy [9] carried out a multidimensional optimization of the in-cylinder tumble

101 motion for an engine featuring hemispherical combustion chamber. They found that large-scale tumbling
102 flow structures, if persistent and coherent, can be effective in the turbulence enhancement at spark timing,
103 provided that they are dissipated right before ignition. In addition, they underlined that the dominant flow
104 structures through the compression phase are significantly different than those occurring in a steady-state
105 intake flow in a flow test rig. This was also remarked in [10]. Berntsson et al. [11] performed engine tests as
106 well as CFD simulations on a 500 cc single-cylinder engine with different tumble levels. A positive effect of
107 increased tumble on efficiency was highlighted, and advantages were also found as far as knock resistance
108 and EGR tolerance are concerned. Similar results are also reported in [12], where the enhancement of
109 tumble intensity led to an extension of the lean burn range of the engine, which in turn allowed a benefit in
110 fuel economy to be achieved. Accordingly, in [13] the increase in tumble allowed the lean operation limit to
111 be extended up to $\lambda = 1.55$, leading to benefits in fuel consumption as well as in NOx and CO emissions. In
112 [14], the effects of tumble combined with EGR on the combustion and emissions in a spark ignition engine
113 were investigated. In addition to the advantages in fuel consumption due to combustion enhancement, it
114 was also pointed out that EGR allows a de-throttling effect to be obtained, which reinforces the fuel
115 consumption reduction. Similarly, in [15] it was evidenced that the intake tumble can extend the allowable
116 EGR rate, thus largely improving its effectiveness in reducing fuel consumption and emissions.
117 Furthermore, the existence of an optimal tumble level can be identified in different engine working
118 conditions, as far as fuel consumption and combustion efficiency are concerned [16]. The synergic effect of
119 tumble enhancement and mixture dilution by EGR in reducing fuel consumption and NOx emissions is also
120 testified in [17]. These effects are largely due to the increase in the flame propagation speed, which is
121 obtained through tumble enhancement. As a matter of fact, in [18] a flame propagation increase by 35%
122 was evidenced, when the non-dimensional tumble was increased from 0.5 to 2.2.

123 Several technical solutions have been proposed for the tumble enhancement in SI engines in the last two
124 decades. The common target of such solutions is the deviation from the flow balance between two halves
125 of the intake valve curtain area. The flow is in fact mostly conveyed to the cylinder through the upper
126 curtain area portion. A few practical examples are the intake valve masking [19], the adoption of restriction

and flow-separating plates [11], the use of an adapter for the intake runner [20], the offset of the intake valve [12] as well as the optimization of the port geometry [21, 22]. The application of a masking surface downstream of the intake valve was also investigated in [23]. However, in this case the flow was inhibited in the upper curtain area portion, so that the so called 'reverse tumble' was promoted. The benefit in terms of turbulence intensity around the spark location was of around 100% with respect to the baseline design. Finally, it is worth pointing out that the turbulence level at spark timing is influenced also by the tumble evolution during intake and compression, which can be affected by the piston shape and position [24].

The present paper aims to give a further contribution to the assessment of design solutions for the tumble improvement, by considering a purposely designed masking surface downstream of the intake valve. The main novelty of the paper is, on one hand, the adoption of very high engine compression ratio (CR) values (as explained in the next section), which determine an apparent influence between the induced tumble and the piston. On the other hand, the combined optimization of the cylinder head design and CR, as well as the correlation between numerical and experimental results, represents an added value.

2. PRESENT WORK

The present paper reports part of the outcomes of a research activity carried out by Politecnico di Torino (PoliTo) and Fiat Research Center (CRF) within the Biomethair regional research project (Automotive platform of Regione Piemonte, Italy, http://www.biomethair.it/index.php). The activity has been aimed at giving a contribution to a new urban-mobility solution with ultra-low environmental impact. This ambitious target has been pursued by means of the development and integration of a number of advanced technologies, including hybrid propulsion, high-performance engines as well as biofuel production and utilization.

The activities performed by PoliTo and CRF have been focused on the development of a high-performance engine specifically dedicated to CNG fueling and featuring a variable valve actuation (VVA) system as well as very high compression ratios. The main engine characteristics are reported in Table 1. The engine is derived

from the production gasoline-fueled TwinAir engine and the compression ratio (CR) was increased from the baseline value of 10 up to the range 12-14, whose optimization was part of the design process. The results of the Biomethair engine development activity are presented in this paper, as well as in [10]. More precisely, the results of the experimental and numerical characterization of the steady-state tumble flow from the Biomethair engine head were presented in [10]. In addition, a numerical model for the engine-cycle transient simulation was developed and preliminarily assessed. The present paper is focused on the design and optimization activity of the Biomethair combustion chamber. The activity was carried out by combining 3D simulation results to performance and emission data from the dyno test rig at CRF.

Table 1 – Biomethair engine characteristics

Feature	**Value/specification**
Displacement [cm^3]	875
Number of cylinders	2
Compression ratio	12-14 (production engine: 10)
Turbocharger	WG-controlled
Target torque	140 Nm @2000 rpm
Target power	60 kW @5000 rpm

3. ENGINE DEVELOPMENT PROCEDURE

The engine development activity described in the present paper is divided into three parts. First, two variants for the cylinder head geometry were considered and compared, with specific reference to their performance in terms of permeability and tumble intensity. More specifically, the influence of a purposely designed masking surface is analyzed through the comparison with the baseline cylinder head configuration without mask. As a matter of fact, as widely discussed in the Introduction section, the enhancement of the tumble intensity caused by the masking wall can lead to an increase in the turbulence intensity and, in turn, to remarkable benefits in terms of combustion speed, efficiency and repeatability. On the other hand, the

presence of an additional obstacle might lead to a detriment in the volumetric efficiency. A steady-state cylinder head numerical model ('virtual flow rig' model), previously developed and validated [10], was applied for this analysis. Second, the selected cylinder head geometry was used to assemble the prototype engine, by considering three different piston variants which corresponded to three different CR values, ranging from 12 to 14. The CR effect was then analyzed by combining experimental and 3D simulation results. Third, the selected compression ratio was finally considered to verify the overall effect of the cylinder head geometry on the in-cylinder tumble, in the presence of combustion.

The baseline versions for the "virtual flow rig" model and the complete engine model adopted in the current study were extensively described and validated in [10], some details are anyhow summarized hereafter for the reader's convenience. The main model features are also summarized in Table 2, along with the associated average calculation time.

Table 2. CFD model summary

	'Virtual flow rig' model	**Engine model**
Cell count	~4,000,000	~800,000 (at BDC)
Cell size	min. 0.3 mm, max. 2.5 mm	min. 0.4 mm, max. 1 mm
Turbulence model	Realizable k-ε	RNG k-ε
Near wall treatment	'Two layer all y+'	Angelberger law of the wall [25]
Combustion model	-	ECFM-3z [26]
Average calculation time	~16h on a 24 CPU workstation	~48h per cycle, on a 24 CPU workstation

The steady-state flow rig model was developed within StarCCM+ v.8.06 and features around 4 million of cells, the mesh size ranging between 1.25-2.5 mm in the intake ports and 0.3 mm in the valve curtain region (Fig. 1a). The Realizable k-ε model turned out to be the best compromise between model accuracy, stability and computational cost, within the Reynolds-Averaged Navier-Stokes (RANS) framework, and was

thus selected for the analyses discussed in the present paper. For the near wall treatment, a two-layer approach named 'all y+' was selected and 5 cell layers were placed at the wall boundaries. Such an approach is claimed to provide a reliable solution in the entire y+ range.

The transient engine model has been developed by means of the commercial code Es-ICE version 4.20 and features around 800 000 cells at bottom dead center, with a cell size between 0.4 and 1 mm (Fig. 1b). The RNG k-ε model was adopted, along with the Angelberger law of the wall [25], with a near wall extrusion layer of 0.2 mm, which insures a y+ value ranging between 30 and 100. The three-zone extended coherent flamelet model (ECFM-3z) [26] was used in order to simulate the in-cylinder combustion process. The potential of the model in the engine simulation have been recently further demonstrated in [27,28], with reference to a dual-fuel, partially stratified, SI combustion. In the present work, the model coefficients were calibrated based on experimental data in seven engine working conditions with different engine compression ratios. A maximum error of 3% and 2 deg CA was detected on peak firing pressure and 'combustion barycenter' (MFB50) position, respectively. An example of comparison between experimental and CFD data is provided in Fig. 2, where an operation point at 3500 rpm, full load (upper row) and another one at 2000 rpm, bmep=4 bar (lower row) are considered. The calibrated model was applied to the different geometry variants under study by keeping the ECFM coefficients unchanged, thus giving consistency to the analysis.

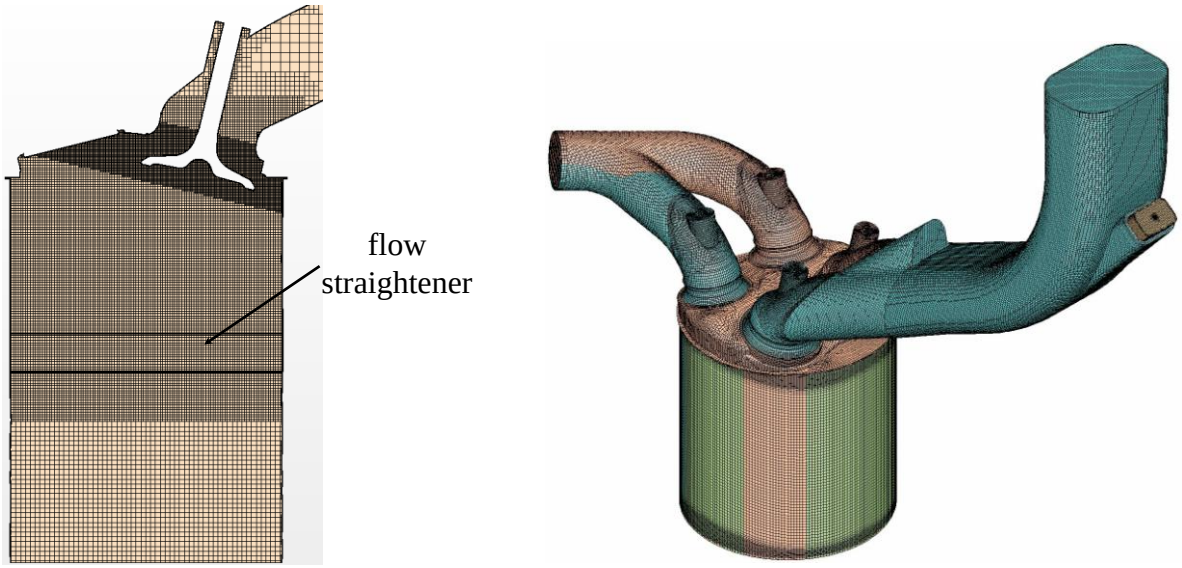

(a) (b)

205

206 Figure 1. CFD numerical models: cross- section of the steady-state cylinder head numerical model ('virtual

207 test rig') (a); full view of the transient engine model (b).

208

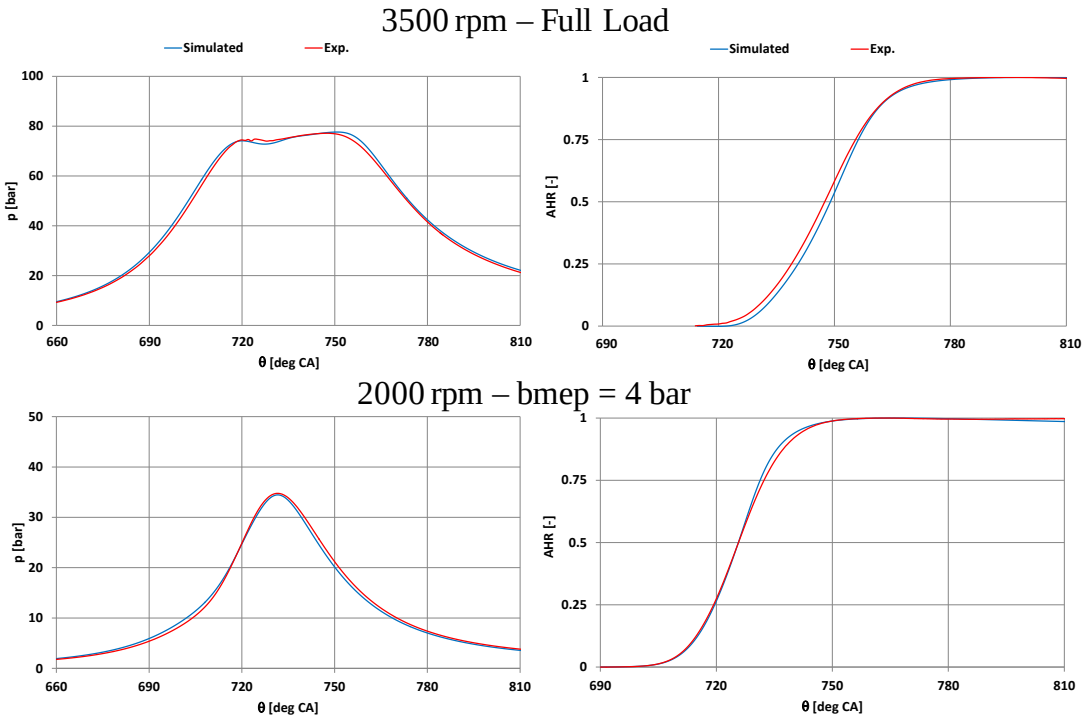

209

210 Figure 2. Engine numerical model validation results: pressure (left) and heat release (right) profiles.

211

4. RESULTS AND DISCUSSION

4.1 Steady-state flow CFD simulation

The first step of the combustion chamber design process was the comparison of two variants for the head dome, which are represented in Fig. 3. In this phase, only the cylinder head is considered, without any piston combined to it, according to the approach of the steady-state cylinder head numerical model (Section 3). The first variant is the baseline one (Fig. 3a), which is adopted in the production gasoline engine. The second variant was obtained by creating a masking wall right downstream of the intake valve, to the wall side, as can be seen in Fig. 3b where the masking wall is highlighted with the red oval. The chamber variants were compared through the simulation of the steady-state flow from the intake valve, by considering the CFD model in Fig. 1a.

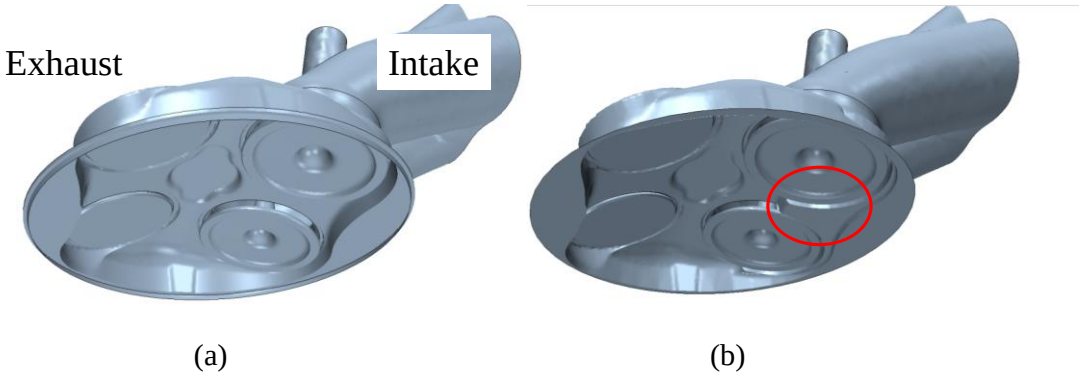

Figure 3. Design variant: baseline without mask (a) and with mask (b).

The results of the comparison are reported in Figs. 4-6. Fig. 4 shows the steady-state velocity field in the intake valve plane, which was obtained from both variants at the intermediate valve lift of 4 mm. Such a lift value is close to the height of the masking surface in the variant with mask. The figure shows that in the baseline configuration the curtain area of the intake valve is almost entirely exploited and inlet velocities of 100-120 m/s can be observed at both sides of the intake valve (Fig. 4a). The overall tumble intensity thus

231 results from the difference in angular momentum contributions of both the 'direct' and the 'reverse'
232 tumble. Conversely, the 'reverse' tumble is obstructed by the presence of the masking wall in the variant
233 with mask, as it is clearly shown in Fig. 4b. In such a case, the negative contribution due to the flow issuing
234 from the intake valve to the wall side is inhibited to a great extent, thus increasing the overall tumble
235 intensity.

236

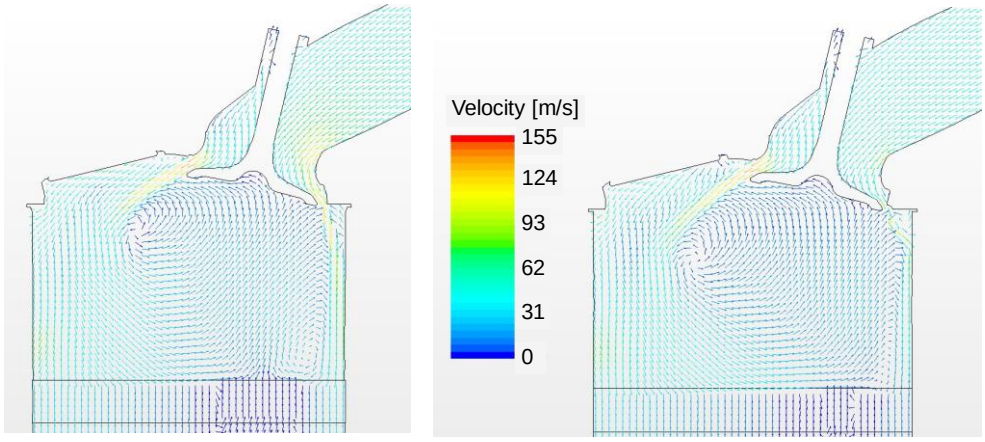

(a) (b)

237

238 Figure 4. Steady state intake velocity field at the intermediate lift of 4 mm: baseline without mask (a) and
239 with mask (b) configurations.

240

241 The effect of the combustion chamber geometry on the valve performance is summarized in Fig. 5 in terms
242 of discharge coefficient and tumble number. The tumble number is given by ([10]):

243 $$N_T = \frac{-\left(\omega_{av,INT} + \omega_{av,EXH}\right) \cdot B}{v_{is}} \qquad (1)$$

244 where $\omega_{av,INT}$ and $\omega_{av,EXH}$ are equivalent angular speed referred to the intake and the exhaust side,
245 respectively (see Fig. 3), according to the equation below:

246 $$\omega_{av,EXH} = \frac{\sum_{e=1}^{N_e} V_{z,e} X_e}{\sum_{e=1}^{N_e} X_e^{\,2}}; \qquad \omega_{av,INT} = \frac{\sum_{i=1}^{N_i} V_{z,i} X_i}{\sum_{i=1}^{N_i} X_i^{\,2}} \qquad (2)$$

247 and v_{is} is the isentropic flow velocity corresponding to the actual pressure ratio. The formulas above are
248 applied with reference to a measurement plane located 2 mm below the flow straightener (Fig. 1a). The
249 position x=0 is the cylinder axis position, and the indices i and e are related to the intake and the exhaust
250 side, respectively. As far as the influence of the chamber design is concerned, for low and intermediate
251 valve lift values the presence of the masking wall gives rise to a decrease of the valve discharge coefficient
252 by around 10-20%, whereas the tumble number is increased up to two-three times its original value, due to
253 the reverse tumble inhibition discussed above. At high lift (above 5 mm), the intake valve results to be
254 displaced beyond the extension of the masking surface, consequently its effect virtually disappears as is
255 testified by the comparable values of both C_D and N_T for the baseline and the 'masked' design.

256

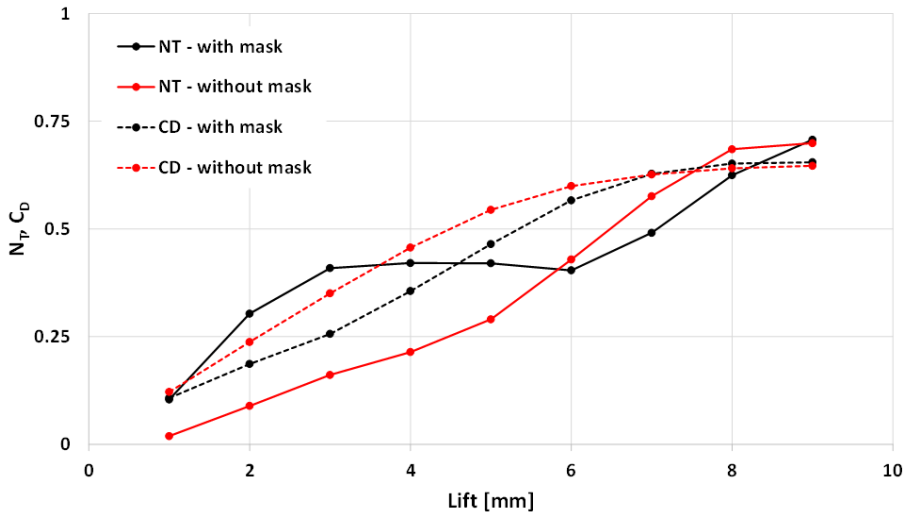

257

258 Figure 5. Tumble number (NT) and discharge coefficient (CD) versus valve lift.

259

The results in Fig. 5 can be used as input to estimate the effect of the mask presence on the global tumble and permeability of the valve in the real engine installation. Following the procedure in [29], with reference to the intake valve lift profile for the considered engine working point, the average discharge coefficient and the steady-state tumble ratio at IVC can be defined as follows:

$$\overline{C_D} = \frac{\int_{\vartheta_1}^{\vartheta_2} C_D \cdot d\vartheta}{\vartheta_2 - \vartheta_1} \tag{3}$$

$$TR = \frac{B \cdot s}{N_v D_v^2} \cdot \frac{\int_{\vartheta_1}^{\vartheta_2} C_D \cdot N_T \cdot d\vartheta}{\left(\int_{\vartheta_1}^{\vartheta_2} C_D \cdot d\vartheta\right)^2} \tag{4}$$

where θ_1 and θ_2 represent the intake valve opening and closure crank angle positions, respectively. The considered coefficients were calculated in three engine working points, as reported in Table 3. The results are reported in Fig. 6. The valve lift profile considered in each of the working points can be found in Fig. 7.

Table 3. Engine working points for tumble ratio evaluation.

Speed [rpm]	**bmep [bar]**
2000	2
2000	4
3500	Full load

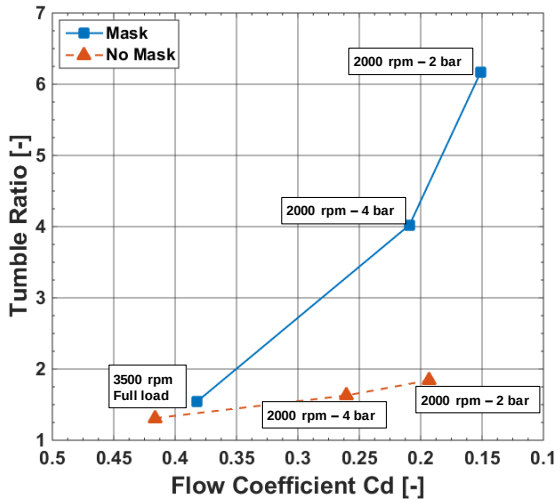

272

273 Figure 6. Average flow coefficient and tumble ratio in different engine working points.

274

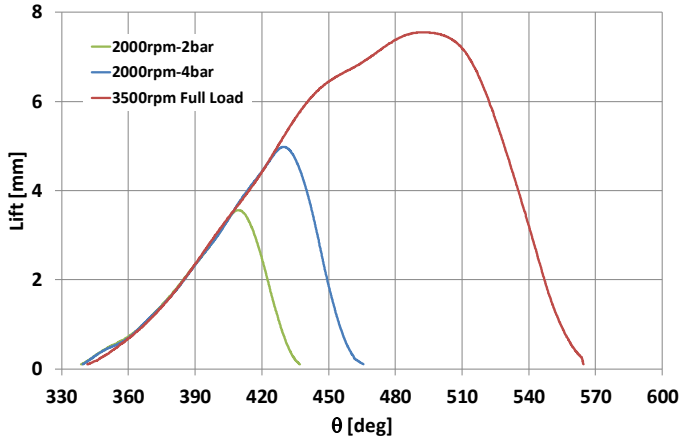

275

276 Figure 7. Valve lift profiles.

277

278 The results in Fig. 6 show that the presence of the mask determines a decrease in the average discharge
279 coefficient by around 20-30%, mainly due to the reduced effective flow area caused by the obstruction
280 effect of the wall. As far as the tumble ratio defined by Eq. 4 is concerned, the effect is actually dependent
281 on the engine load. At partial load, the valve opening time and maximum lift are highly reduced by the
282 action of the VVA device (Fig. 7). Consequently, the valve position is kept within the range corresponding to
283 the extension of the masking surface, thus maximizing its effect on the flow unbalance. As a matter of fact,

284 the tumble ratio at partial load is increased by 150% in the 2000rpm-4bar working point, and by 235% in
285 the 2000rpm-2bar one. At full load, the valve lift is kept above 5 mm for about half of the total opening
286 time. It is worth recalling that the mask is virtually ineffective in for high lift, and observing that such lift
287 values affect the integral at the numerator of Eq. 4 to a great extent, due to the high value of C_D in that
288 range. For this reason, the tumble ratio benefit is limited to 18%. Although the tumble ratio estimated by
289 steady-state flow data might not be fully representative of the flow behavior in the real engine [10], their
290 significance is usually sufficient to assess for the suitability of steady flow tests during the early design
291 stages of tumble-generating induction systems [29]. Consequently, based on the results discussed above, it
292 was decided to adopt the configuration with mask for assembling the Biomethair engine prototype, given
293 the minor penalty in the discharge coefficient which accompanies the remarkable tumble increase

294

295 **4.2 Experimental tests**

296 The experimental results presented in this paper were acquired by CRF and shared with Politecnico di
297 Torino within the Biomethair project. Three values of the compression ratio (namely, 12, 13 and 14) were
298 actually tested, by assembling different piston design variants with the same cylinder head (see Fig. 3). The
299 piston design variants are represented in Fig. 8. The tests aimed at defining the optimal engine CR as a
300 compromise between performance at full load and fuel consumption at partial load.

301

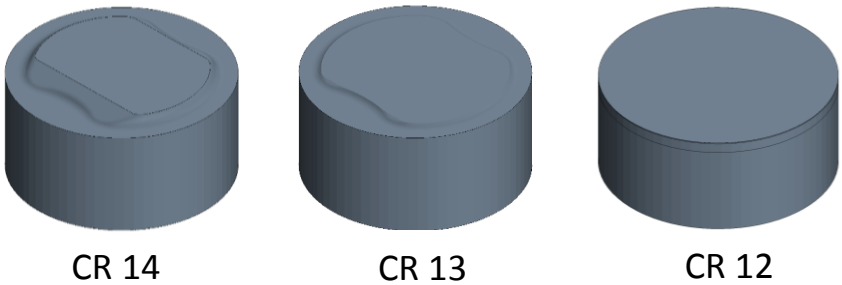

302

303 Figure 8. Piston shapes corresponding to the considered compression ratio values.

Figs. 9 and 10 show the results obtained at full load for the three compression ratios. More specifically, Fig. 9 compares the torque and power curves obtained with the three considered CR to the reference curve of the normal production (NP) engine, whereas Fig. 10 reports the CoV of the imep, the ensemble-averaged peak firing pressure (PMAX0) and the maximum cycle resolved peak firing pressure (PMAXmx). In all the cases, the engine calibration was aimed at maximizing the engine load, by taking the compressor surge limit into account. Moreover, the threshold for the ensemble value of the peak firing pressure was set at 85 bar, allowing the single 'upper' cycles to reach 100 bar. Such limits led to the limitation of the spark advance (SA) to 5-6 deg CA in most cases. The target performance data were set at 140 Nm and 60 kW. The results showed that the target torque value is achieved with all the CRs. However, the higher one (CR=14) does not allow the power target to be fulfilled. As far as the cyclic variation of the engine is concerned, an increasing trend of the imep coefficient of variation against CR was found (Fig. 10). This is due to the combination of two effects. First, as CR is increased, the spark timing (ST) had generally to be reduced to keep the peak firing pressure (PFP) within its limit. Second, for a given ST, the increase in CR negatively affects the combustion regularity. This is to be ascribed to the detriment in the tumble intensity evolution during the intake and the compression stroke, as will be shown in Section 4.3, and is evidenced in Fig 11. In the figure, the in-cylinder pressure acquisitions are showed for different CR values in the operating point at 3500 rpm, full load, with the same SA setting. The pressure traces pertaining to individual cycles are represented by light gray lines, whereas the red thick lines show the results of the ensemble average of acquired cycles. The red, dashed line indicates the angular position of the spark timing. As can be seen, the in-cylinder pressure at spark timing increases as CR increases. Moreover, the cycle-resolved pressure traces show a higher dispersion in the CR=14 case, which features both very fast combustion events and misfire cycles. It is thus necessary to further reduce the spark timing in order to reduce the PFP of fast burning cycles. Although the precise control of the limit on the maximum cycle-resolved PFP was rather difficult, and thus the threshold of 100 bar was slightly exceeded in many cases, the obtained results can be considered acceptable as far as the structural integrity of the engine is concerned.

330

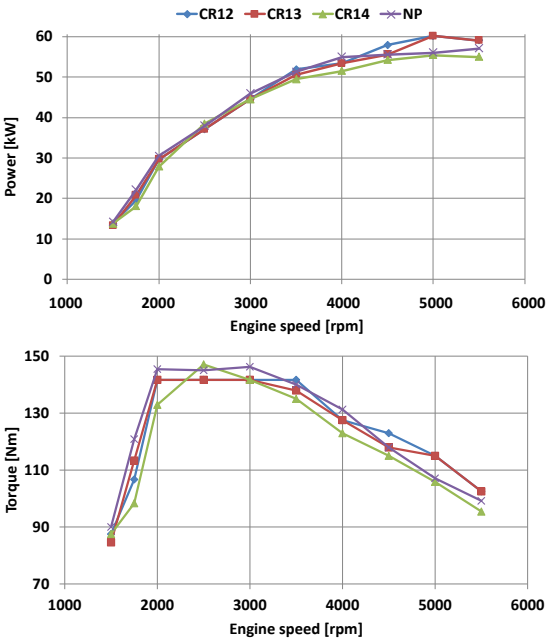

331

332 Figure 9. Full load performance curves for the three CR values compared to NP engine.

333

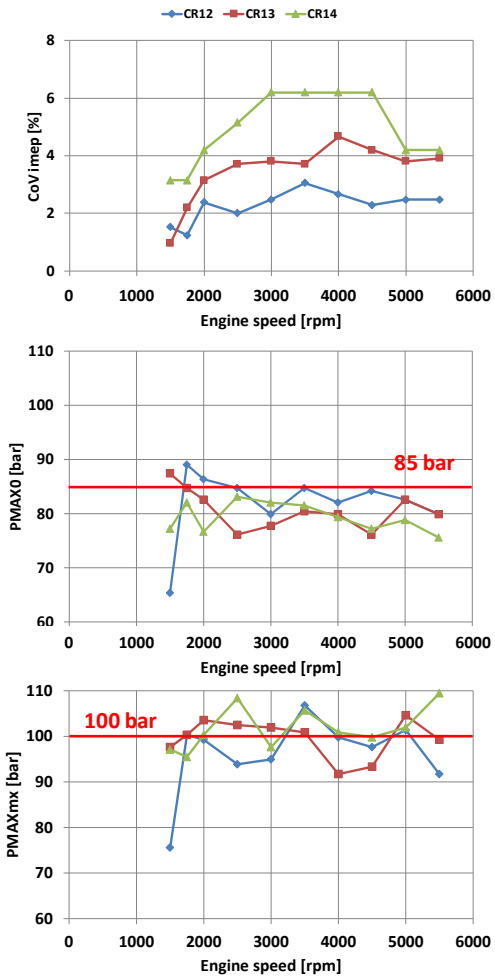

334

335 Figure 10. Full load performance curves: CoV imep, average PFP (PMAX0) and maximum cycle-resolved PFP

336 (PMAXmx).

337

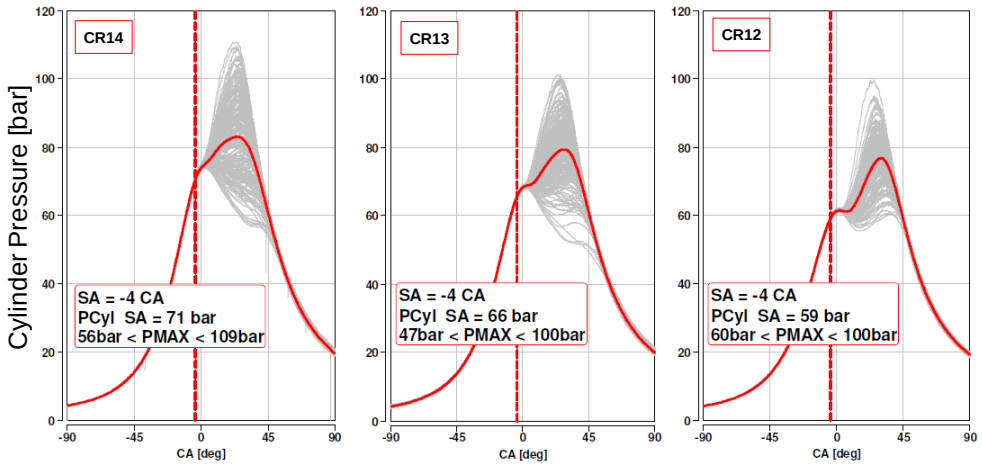

338

339 Figure 11. Cycle-by-cycle and average in-cylinder pressure at 3500 rpm, Full load, for CR=14 (left), CR=13
340 (middle) and CR=12 (right).

341

342 The CR effect on engine performance and efficiency was also investigated at partial load. The engine was
343 run in a few selected working points, as detailed in Table 4.

344

345 Table 4. Engine working points for experimental tests at partial load.

Speed [rpm]	**bmep [bar]**
1500	2, 6
2000	2, 3, 4, 6, 8
2500	2, 4, 8, 12
3000	8, 12, 15

346

347 The results are presented in Figs. 12 and 13. Fig. 12 shows the engine bsfc reduction, with respect to the
348 base engine with CR=10. As a matter of fact, as CR increases, the efficiency of the reference
349 thermodynamic Otto cycle increases. However, the impact of the thermodynamic losses due to imperfect
350 or untimely combustion process might affect the overall engine behavior. At partial load, no issues about
351 the PFP limit arise, thus the combustion timing can be always set to its optimal value (usually corresponding
352 to MFB50 ranging from 5 to 10 deg after top dead center), corresponding to the maximum brake torque
353 (MBT) conditions. Consequently, the effect of combustion untimeliness is similar for the three CR values,
354 and the dominant effect is given by the increase in the Otto cycle efficiency. Consistently, a benefit in
355 engine fuel consumption was obtained experimentally in almost all the working points at it is shown in Fig.
356 12. The impact of the engine CR on the combustion cycle-to-cycle variation is represented in Fig. 13 for a
357 few selected engine operating conditions, amongst those included in Table 4. Similarly to the full load case,

the combustion process gets less regular as CR increases, again suggesting that a detriment in the turbulence level at combustion start has occurred.

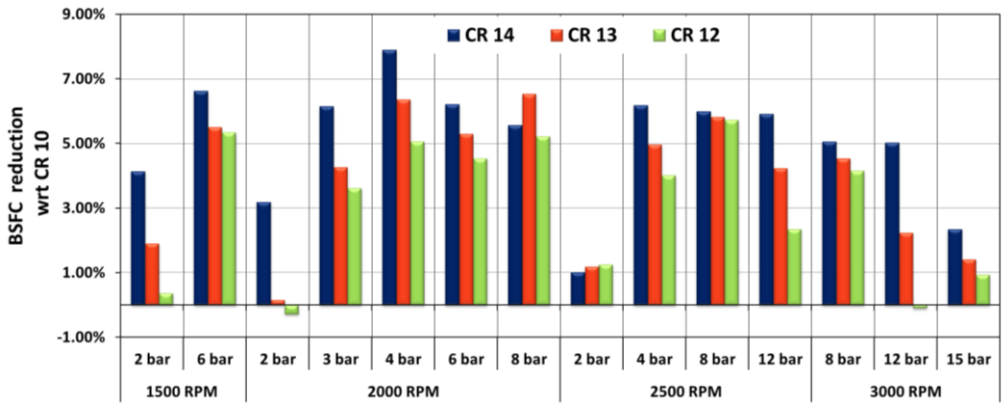

Figure 12. Percentage bsfc reduction with respect to the baseline engine with CR=10, for various working points at MBT timing.

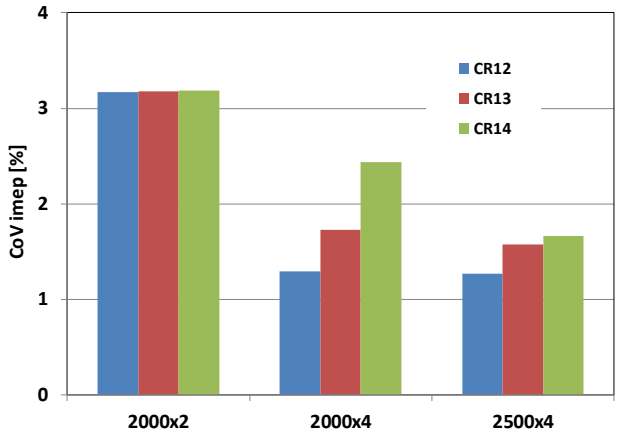

Figure 13. CoV imep in a few selected working points for the different CRs.

The experimental activity carried out by CRF evidenced the following main effects as the compression ratio is increased:

1. The maximum engine power decreases;

2. The bsfc at partial load decreases;
3. The benefit in bsfc at full load are hidden by the non-optimal combustion timing, mainly due to the occurrence of the PFP limitations;
4. The cycle-to-cycle variability of combustion increases both at partial load and at full load.

The CR=13 value was finally selected for equipping the demonstrator vehicle, as the best compromise between fuel consumption at partial load, combustion quality and engine performance at full load.

4.3 Engine transient CFD simulations

A set of CFD simulations was planned aside the experimental activity, focused on investigating the in-cylinder flow and combustion process in the engine cycle. The work was aimed at giving a deeper insight to the combustion behavior in the engine propotype, as well as at verifying the consistency of the steady-state flow simulation results as far as the effect of the masking surface is concerned.

First of all, as a dependence of the combustion speed and cycle-to-cycle variation on the CR was observed, as it is shown in Section 4.2, the engine configuration with mask was simulated with different compression ratio values in order to have an insight into the tumble and turbulence evolution. The results are shown in Figs. 14-15. Fig. 14 reports the in-cylinder velocity field at an intermediate instant of the induction stroke, with reference to the combustion chamber variant with mask. As a matter of fact, for a given crank angle a difference in CR (and, in turn, in the clearance volume) gives rise to a different position of the piston top with respect to the cylinder head. In the CR=14 case, the piston is closer to the head and the intake flow impinges on it, resulting in a decrease in the tumble vortex size and reduction of its overall intensity. Contrariwise, in the lower compression ratio case, the resultant size of the direct tumble structure is bigger and better defined. Fig. 15 shows the tumble number and the mass-averaged turbulence intensity evolution versus crank angle, for the three CR values at 3500 rpm and full load. The in-cylinder tumble number is given by:

$$TN = \frac{\int_{m_{cyl}} \left[-v_z \left(x - x_m \right) + v_x \left(z - z_m \right) \right] \cdot dm_{cyl}}{\frac{2\pi N}{60} \int_{m_{cyl}} \left[\left(x - x_m \right)^2 + \left(z - z_m \right)^2 \right] \cdot dm_{cyl}} \quad (5)$$

where v_x, v_z are the x- and z- components of the velocity, x_m, z_m are the x- and z- coordinates of the cylinder center of mass and N is the engine speed in rpm. As the piston exerts a disturbance effect on the direct tumble vortex throughout the first part of the induction stroke, the TN generation is the higher in the CR=12 case. This happens between around 360 and 450 deg CA, and is the cause of the difference in the TN curves, which can be appreciated in Fig. 15. The higher tumble strength in the case with CR=12 in turn determines a higher turbulence level (by around 20%) in correspondence to the spark timing, hence contributing to the explanation of the observed differences in the combustion speed and stability (Figs. 10, 11 and 13).

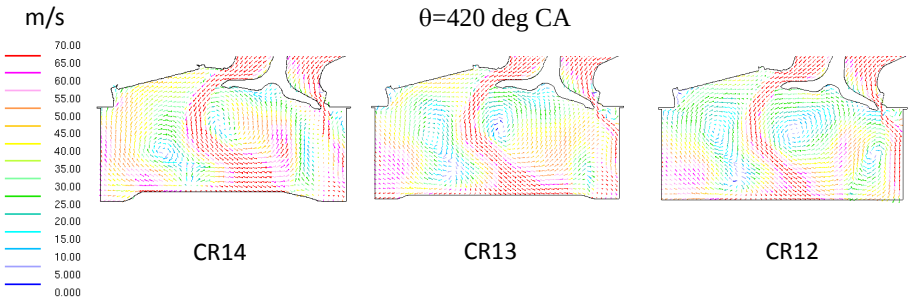

Figure 14. In-cylinder velocity field during the intake stroke for different CR values – 3500 rpm, Full load.

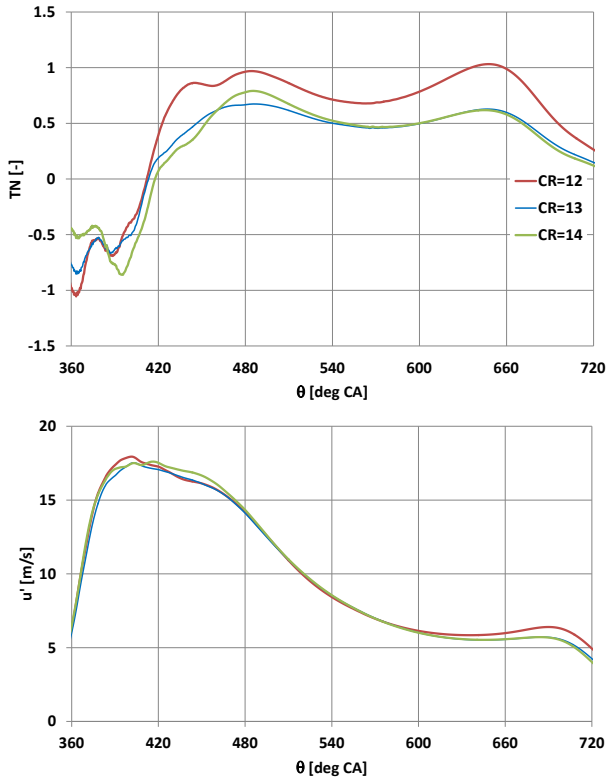

408

409 Figure 15. Tumble number and mass-averaged turbulence intensity versus crank angle – 3500 rpm, Full

410 load.

411

412 Further simulation work was carried out, in order to assess for the differences in fluid-dynamic and

413 turbulence flow features between the baseline configuration and the one with masked intake valve. Fig. 16

414 shows the effect of the combustion chamber variants on the in-cylinder flow field structure at 450 deg CA,

415 for the working point at 2000 rpm and 4 bar, with CR=13. As discussed above, the piston presence affects

416 the overall size of the direct tumble vortex, however the relative effect between the configuration without

417 mask and that with mask is qualitatively the same as the one observed in the steady-state analysis (see Fig.

418 4). In the considered working point, the actuated valve lift profile is represented by the blue line in Fig. 7.

419 Since the maximum lift is kept within the size of the masking wall, the latter is able to exert its influence

420 over the whole intake process. Consequently, a remarkable benefit is obtained in terms of both tumble

421 number and turbulence as can be inferred from Fig. 17. In correspondence to the spark timing position

422 (about 690 deg CA) an increase by around 90% and 10% have been obtained for TN and for the turbulence

intensity, respectively, relative to the baseline variant. As far as the full-load conditions are concerned, a considerably lower effect is obtained, due to the higher inlet valve lift. In fact, as discussed in Section 4.1, the masking surface is virtually ineffective when the valve lift is greater than the surface extension. Fig. 18 shows an overall evaluation of the mask effect, including full-load as well as partial load cases, for CR=12 and CR=13. As can be seen in the figure, with the exception of the full load case with CR=13, the presence of the mask increases the tumble level in the cylinder and, in turn, the turbulence intensity. However, at a first sight a detriment in tumble was also obtained in the 2000 rpm, bmep=2 bar case with CR=12. Still, in such a case the virtually nil TN is actually the result of the compensation of two opposite moment contributions and does not represent a penalty, as it is confirmed by the comparable turbulence level obtained. Concerning the turbulence effect on burning speed, except the CR=13 configuration at full load conditions, a benefit on the combustion duration from 1% to 50% of heat released (MFB1-50) between 2 and 6 deg CA was found. This is in agreement with the observed experimental combustion behavior, also from the point of view of the cycle-to-cycle stability, and confirms the overall benefit that is obtained by adopting the tumble oriented cylinder head design.

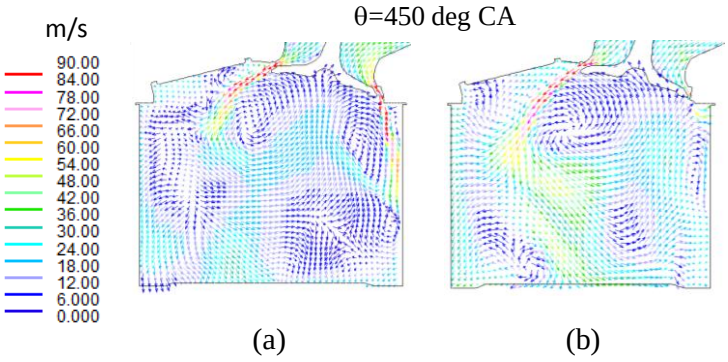

Figure 16. Effect of the intake valve masking surface on in-cylinder flow field at 2000 rpm, bmep=4 bar.

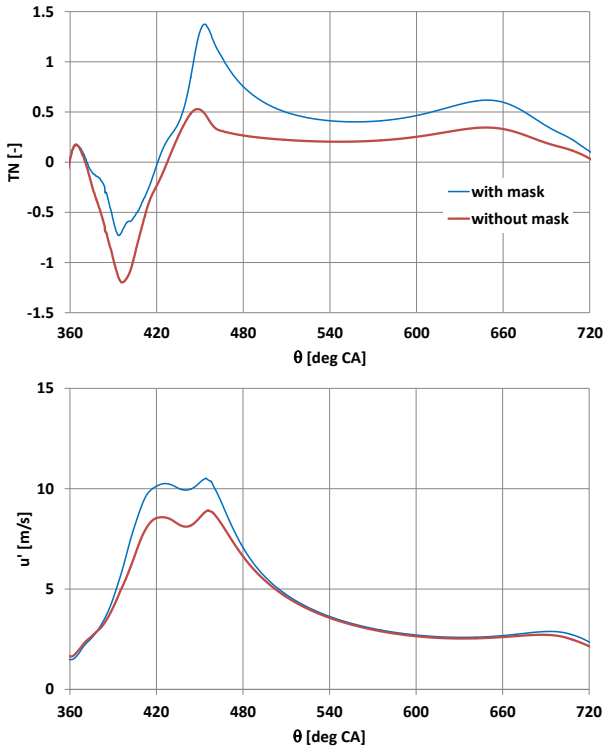

441

442 Figure 17. Tumble number and turbulence evolution versus crank angle for the variants with and without

443 mask – 2000 rpm, bmep=4 bar.

444

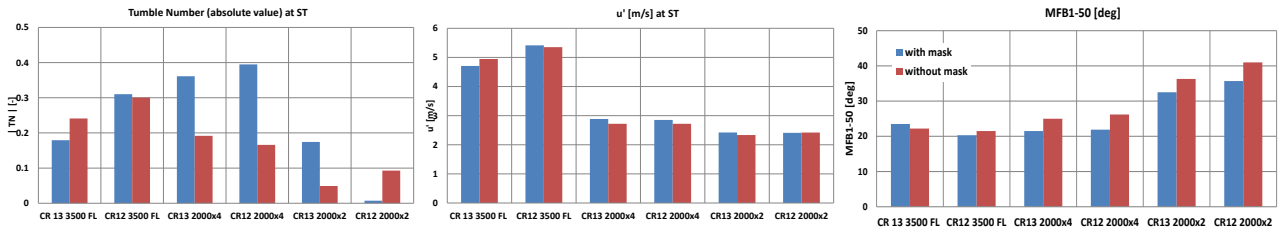

445

446 Figure 18. Tumble number, turbulence intensity and MFB1-50 combustion interval for the variants with and

447 without mask.

448

449 **6. CONCLUSION**

450 The activity presented in this paper was focused on the development of a monofuel, high performance, NG

451 engine. More specifically, the design of the engine combustion chamber was described, with reference to

452 the optimization of the engine CR and to the trade-off between engine permeability and tumble
453 characteristics of the intake port. The activity was carried out by combining 3D simulations and
454 experimental tests. The main conclusions are as follows.

455 – The steady-state simulations indicated that the engine configuration with mask features a decrease
456 in the average discharge coefficient by around 20-30%, whereas an increase in the tumble ratio by
457 around 200% is obtained at partial load.
458 – The simulations of the engine cycle led to the same conclusion from a qualitative point of view,
459 though the presence of the piston modifies the tumble intensity of the induced flow with respect to
460 the 'undisturbed' flow in the virtual steady-state flow rig. In the 2000x4 working point, the increase
461 in the tumble number at spark timing was of around 90%, which lead to a 10% increase of the
462 turbulence intensity.
463 – Overall, the presence of the masking surface determined a benefit in the turbulence intensity at
464 spark timing in almost all the cases at partial load, and a reduction of the MFB1-50 interval
465 between 2 and 6 deg CA was correspondingly obtained.
466 – With reference to the optimization of the engine CR, the experimental activity carried out at CRF
467 showed that CR=13 was the best compromise between fuel consumption at partial load, engine
468 performance at full load, and combustion quality.
469 – The cycle-to-cycle variability of combustion increased with the increase in the engine CR, due to the
470 detriment of the tumble number and of the turbulence intensity. The latter is higher by around
471 20% in the CR=12 case.
472

473 **7. ACKNOWLEDGEMENTS**

474 Financial support to this activity has been provided within the Biomethair regional research project
475 (Automotive platform of Regione Piemonte, Italy). The authors warmly thank Giorgio Carpegna, Andrea
476 Gerini, Francesco Perna, Andrea Stroppiana of Centro Ricerche Fiat S.C.p.A. for their valuable support.

8. REFERENCES

1. Maclean HL, Lave LB. Evaluating automobile fuel/propulsion system technologies. Prog Energy Combust Sci 2003;29: 1–69.
2. Baratta M, Misul D. Development of a method for the estimation of the behavior of a CNG engine over the NEDC cycle and its application to quantify for the effect of hydrogen addition to methane operations. Fuel 2014; 140: 237-249.
3. Bergthorson JM, Thomson JM. A review of the combustion and emissions properties of advanced transportation biofuels and their impact on existing and future engines. Renewable and Sustainable Energy Reviews 2015 (42): 1393–1417.
4. Cucchiella F, D'Adamo I. Technical and economic analysis of biomethane: A focus on the role of subsidies. Energy Conversion and Management 2016 (119): 338–351.
5. E. Porpatham, A. Ramesh, B. Nagalingam, Investigation on the effect of concentration of methane in biogas when used as a fuel for a spark ignition engine, Fuel, Volume 87, Issues 8–9, July 2008, Pages 1651-1659, ISSN 0016-2361.
6. R. Chandra, V.K. Vijay, P.M.V. Subbarao, T.K. Khura, Performance evaluation of a constant speed IC engine on CNG, methane enriched biogas and biogas, Applied Energy, Volume 88, Issue 11, November 2011, Pages 3969-3977, ISSN 0306-2619.
7. Baratta M, d'Ambrosio S, Misul D, Spessa E. Effects of H2 Addition to CNG Blends on Cycle-To-Cycle and Cylinder-to-Cylinder Combustion Variation in an SI Engine. J. Eng. Gas Turbines Power 136(5), 051502 (Jan 02, 2014) doi:10.1115/1.4026163.
8. Fanhua Ma, Mingyue Wang, Long Jiang, Jiao Deng, Renzhe Chen, Nashay Naeve, Shuli Zhao, Performance and emission characteristics of a turbocharged spark-ignition hydrogen-enriched compressed natural gas engine under wide open throttle operating conditions, International Journal of Hydrogen Energy, Volume 35, Issue 22, November 2010, Pages 12502-12509, ISSN 0360-3199.

9. Amer AA, Reddy TN. Multidimensional Optimization of In-Cylinder Tumble Motion for the New Chrysler Hemi. SAE Tech Paper 2002-01-1732, 2002.
10. Baratta M, Misul D, Spessa E, et al. Experimental and numerical approaches for the quantification of tumble intensity in high-performance SI engines. Energy Conversion and Management 138, pp. 435–451, 2017. http://dx.doi.org/10.1016/j.enconman.2017.02.018.
11. Berntsson A, Josefsson G, Ekdahl R, Ogink R, et al. The Effect of Tumble Flow on Efficiency for a Direct Injected Turbocharged Downsized Gasoline Engine. SAE Int. J. Engines 4(2):2298-2311, 2011. https://doi.org/10.4271/2011-24-0054.
12. Saito H, Shirasuna T, Nomura T. Extension of Lean Burn Range by Intake Valve Offset. SAE Int. J. Engines 6(4):2072-2084, 2013. https://doi.org/10.4271/2013-32-9032.
13. Zhou F, Fu J, Ke W, et al. Effects of lean combustion coupling with intake tumble on economy and emission performance of gasoline engine. Energy 133:366-379, 2017.
14. Zhang Z, Zhang H, Wang T, et al. Effects of tumble combined with EGR (exhaust gas recirculation) on the combustion and emissions in a spark ignition engine at part loads, Energy 65, 1: 18-24, 2014.
15. Fu J, Zhu G, Zhou F, et al. Experimental investigation on the influences of exhaust gas recirculation coupling with intake tumble on gasoline engine economy and emission performance. Energy Conversion and Management 127 (2016): 424-436.
16. Ogink R, Babajimopoulos A. Investigating the Limits of Charge Motion and Combustion Duration in a High-Tumble Spark-Ignited Direct-Injection Engine. SAE Int. J. Engines 9(4):2129-2141, 2016. https://doi.org/10.4271/2016-01-2245.
17. Fu J, Zhu G, Zhou F, et al. Experimental investigation on the influences of exhaust gas recirculation coupling with intake tumble on gasoline engine economy and emission performance. Energy Conversion and Management 127: 424–436, 2016.
18. Yang J, Dong X, Wu Q, Xu M. Effects of enhanced tumble ratios on the in-cylinder performance of a gasoline direct injection optical engine. Applied Energy 236: 137–146, 2019.
19. Iyer C, and Yi J. 3D CFD Upfront Optimization of the In-Cylinder Flow of the 3.5L V6 EcoBoost Engine. SAE Tech Paper 2009-01-1492, 2009. https://doi.org/10.4271/2009-01-1492.

20. Takahashi D, Nakata K, Yoshihara Y, Omura T. Combustion Development to Realize High Thermal Efficiency Engines," SAE Int. J. Engines 9(3):2016. doi:10.4271/2016-01-0693.
21. Sun Y, Wang T, Lu Z, et al. The Optimization of Intake Port using Genetic Algorithm and Artificial Neural Network for Gasoline Engines. SAE Tech Paper 2015-01-1353, 2015. doi:10.4271/2015-01-1353.
22. Abidin Z, Hoag K, Mckee D, Badain N. Port Design for Charge Motion Improvement within the Cylinder. SAE Tech Paper 2016-01-0600, 2016. https://doi.org/10.4271/2016-01-0600.
23. Millo F, Luisi S, Borean F, Stroppiana A. Numerical and experimental investigation on combustion characteristics of a spark ignition engine with an early intake valve closing load control. Fuel 121:298-310, 2014.
24. Sagaya Raj A, Maharudrappa Mallikarjuna J, Ganesan V. Energy efficient piston configuration for effective air motion – A CFD study. Applied Energy 102: 347-354, 2013.
25. Angelberger C, Poinsot T, Delhay, B. Improving near-wall combustion and wall heat transfer modeling in SI engine computations. SAE Tech Paper 972881; 1997.
26. Colin O, Benkenida A. The 3-Zones Extended Coherent Flame Model (ECFM-3z) for Computing Premixed/Diffusion Combustion. Oil & Gas Science and Technology - Rev. IFP 59 (6) 593-609, 2004.
27. Huang Y, Hong G, Huang R. Numerical investigation to the dual-fuel spray combustion process in an ethanol direct injection plus gasoline port injection (EDI + GPI) engine. Energy Conversion and Management 92: 275–286, 2015.
28. Huang Y, Hong G, Huang R. Effect of injection timing on mixture formation and combustion in an ethanol direct injection plus gasoline port injection (EDI+GPI) engine. Energy 111: 92-103, 2016.
29. Arcoumanis C, Hu Z, Whitelaw JH. Steady flow characterization of tumble-generating four-valve cylinder heads. Proc of Instit Mech Eng, Part D: J of Automobile Eng 207: 203-210, 1993.

Combustion chamber design for a high-performance natural gas engine: CFD modeling and experimental investigation

Mirko Baratta, Daniela Misul, Ludovico Viglione, Jiajie Xu

ANSWER TO REVIEWERS' AND EDITOR'S COMMENTS

Reviewer #4

Authors have made a lot efforts to address the reviewers' comments and the quality of paper has been improved. I recommend publication after a 'minor revision':
Thank you very much for the appreciation of our efforts.

1. Avoid using abbreviations in the title, CFD is well known but NG is not.
As requested, 'NG' has been replaced with 'natural gas' in the paper title.

2. Abstract is usually in one paragraph. I recommend combine the two paragraphs into one, and shorten the background information a little bit.
The abstract has been revised considering the Reviewer's comment.

3. Please hide the outer borders of Figs. 5 and 7. In addition, right side border of Fig. 13 is missing.
The borders of the figures 5, 7 and 13 have been fixed, thank you.

*Revised Manuscript with changes marked

Combustion chamber design for a high-performance natural gas~~NG~~ engine: CFD modeling and experimental investigation

Mirko Baratta, Daniela Misul, Ludovico Viglione, Jiajie Xu
Dipartimento Energia, Politecnico di Torino – Torino, Italy

ABSTRACT

The present paper ~~describes a part of a research activity aimed at giving a contribution to a solution for urban mobility with very low environmental impact, through the development and integration of a number of advanced technologies. The activity have been~~is focused on the development of a high-performance, monofuel, spark ignition engine running on natural gas, featuring a high volumetric compression ratio and a variable valve actuation system ~~for the air metering~~. More specifically, ~~the paper is focused on the analysis of~~ the cylinder head geometry effect has been analyzed and the compression ratio ~~optimization~~has been optimized by means of ~~. S~~steady-state and transient simulation activity, as well as of an extensive experimental campaign~~, were carried out with this purpose~~. The compression ratio effect was mainly investigated by means of experimental tests but a few 3D simulations were also run in order to quantify its impact on the in-cylinder tumble and turbulence. The main novelty of the paper are, first, the adoption of very high engine compression ratio values, second, the combined optimization of the cylinder head design and compression ratio. The main results can be summarized as follows. The engine configuration with mask showed a decrease in the average discharge coefficient by 20-30% and an increase in the tumble ratio by around 200% at partial load. Moreover, the simulation of the engine cycle indicated that the presence of the piston modifies the tumble structure with respect to the steady-state simulation case. An increase in the tumble number and turbulence intensity by around 90% and 10%, respectively, are obtained for the case with mask at 2000 rpm and 4 bar. With reference to the combustion duration, on an average, the presence of the masking surface led to a reduction of the combustion duration (from 1% to 50% of mass fraction burned) between 2 and 6 degrees. As far as the engine compression ratio is concerned, the value of 13 was finally selected as the best compromise between combustion variability, engine performance at full load and fuel consumption at partial load.

KEYWORDS

Natural gas, SI engines, Tumble flow, CFD simulation.

NOMENCLATURE

B	cylinder bore
bmep	brake mean effective pressure
CA	crank angle
C_D	discharge coefficient

CFD	computational fluid dynamics
CNG	compressed natural gas
CoV	coefficient of variation
CR	compression ratio
deg	degree
ECFM	extended coherent flamelet model
EGR	exhaust gas recirculation
GHG	greenhouse gases
imep	indicated mean effective pressure
k	turbulent kinetic energy
MBT	maximum brake torque
MFB	mass-fraction burned
MFB1-50	combustion duration from 1% to 50% of heat released
MFB50	'combustion barycenter' position
NG	natural gas
N_T	tumble number
PFP	peak firing pressure
PMAX0	ensemble-averaged peak firing pressure
PMAXmx	maximum cycle-resolved peak firing pressure
SI	spark ignition
TN	in-cylinder tumble number
TR	tumbling ratio
v_{is}	isentropic flow velocity
VVA	variable valve actuation
x	coordinate for tumble moment of momentum calculation
y+	normalized distance from wall

Greek symbols

ε	turbulence dissipation rate
θ	crank angle position
$\omega_{AV,EXH}$	equivalent angular speed to the exhaust side
$\omega_{AV,INT}$	equivalent angular speed to the intake side

1. INTRODUCTION

Nowadays, the design of modern internal combustion (IC) engines represents a challenging task, due to the raising concern for the global warming as well as to the stringent constraints set by the current pollutant regulations. The use of gasoline or diesel in internal combustion engines is likely to remain the most cost-effective overall ground-based transportation propulsion system for the near future. Furthermore, hybrid and electric vehicles are gaining considerable market share. However, as far as IC engines are concerned, natural gas (NG) represents a factual alternative to traditional fuels thanks to the reduced pollutant and carbon dioxide emissions [1,2]. Moreover, the development of engines compatible with biofuels (for example, natural gas from biomasses) can provide enormous benefits compared to fossil fuels, in terms of greenhouse gases (GHG) emissions [3,4], although attention has to be paid to the fuel properties and their dependence on the blend composition. With specific reference to natural gas, the effect of biogas

composition on the engine operating characteristics has been widely studied by the researchers. In [5] it was found that methane concentration in the biogas significantly improves performance and reduces emissions of hydrocarbons. The lean operation limit is also extended. Similarly, investigations carried out in [6] showed that the methane-enriched biogas performed similarly to compressed natural gas (CNG). Along with methane, other inert species, such as carbon dioxide and nitrogen, can be present in the biogas composition. Furthermore, hydrogen derived from biomass gasification can be blended to natural gas as an additive. As a matter of fact the high speed of flame propagation of hydrogen improves the stability of the combustion process when added to natural gas [7,8].

The development of highly efficient engines cannot withstand the adoption of advanced design methods. As a matter of fact, the introduction of advanced engine concepts, such as, variable valve actuation, turbocharging or direct injection leads to an increase in the complexity of the engine design process, as the number of the design variables is remarkably higher. Moreover, with reference to biofuels dedicated control algorithms might be necessary to make up for the variability in the fuel properties due to the dispersion in the blend composition. As far as the optimization of the combustion chamber and the intake port geometry is concerned, the adoption of computational fluid dynamics (CFD) represents an effective means to support the design process, allowing the time and cost of the associated experimental activity to be reduced. Appreciable benefits in terms of combustion stability, efficiency and pollutant emissions can be obtained if a suitable intensity of swirl and/or tumble motion is targeted. With specific reference to spark ignition (SI) engines, the tumble motion is usually generated in order to increase the turbulence level in the combustion chamber, thus enhancing the combustion stability and the exhaust gas recirculation (EGR) tolerance. Amer and Reddy [9] carried out a multidimensional optimization of the in-cylinder tumble motion for an engine featuring hemispherical combustion chamber. They found that large-scale tumbling flow structures, if persistent and coherent, can be effective in the turbulence enhancement at spark timing, provided that they are dissipated right before ignition. In addition, they underlined that the dominant flow structures through the compression phase are significantly different than those occurring in a steady-state intake flow in a flow test rig. This was also remarked in [10]. Berntsson et al. [11] performed engine tests as well as CFD simulations on a 500 cc single-cylinder engine with different tumble levels. A positive effect of increased tumble on efficiency was highlighted, and advantages were also found as far as knock resistance and EGR tolerance are concerned. Similar results are also reported in [12], where the enhancement of tumble intensity led to an extension of the lean burn range of the engine, which in turn allowed a benefit in fuel economy to be achieved. Accordingly, in [13] the increase in tumble allowed the lean operation limit to be extended up to $\lambda = 1.55$, leading to benefits in fuel consumption as well as in NOx and CO emissions. In [14], the effects of tumble combined with EGR on the combustion and emissions in a spark ignition engine were investigated. In addition to the advantages in fuel consumption due to combustion enhancement, it was also pointed out that EGR allows a de-throttling effect to be obtained, which reinforces the fuel consumption reduction. Similarly, in [15] it was evidenced that the intake tumble can extend the allowable EGR rate, thus largely improving its effectiveness in reducing fuel consumption and emissions. Furthermore, the existence of an optimal tumble level can be identified in different engine working conditions, as far as fuel consumption and combustion efficiency are concerned [16]. The synergic effect of tumble enhancement and mixture dilution by EGR in reducing fuel consumption and NOx emissions is also testified in [17]. These effects are largely due to the increase in the flame propagation speed, which is obtained through tumble enhancement. As a matter of fact, in [18] a flame propagation increase by 35% was evidenced, when the non-dimensional tumble was increased from 0.5 to 2.2.

Several technical solutions have been proposed for the tumble enhancement in SI engines in the last two decades. The common target of such solutions is the deviation from the flow balance between two halves

of the intake valve curtain area. The flow is in fact mostly conveyed to the cylinder through the upper curtain area portion. A few practical examples are the intake valve masking [19], the adoption of restriction and flow-separating plates [11], the use of an adapter for the intake runner [20], the offset of the intake valve [12] as well as the optimization of the port geometry [21, 22]. The application of a masking surface downstream of the intake valve was also investigated in [23]. However, in this case the flow was inhibited in the upper curtain area portion, so that the so called 'reverse tumble' was promoted. The benefit in terms of turbulence intensity around the spark location was of around 100% with respect to the baseline design. Finally, it is worth pointing out that the turbulence level at spark timing is influenced also by the tumble evolution during intake and compression, which can be affected by the piston shape and position [24].

The present paper aims to give a further contribution to the assessment of design solutions for the tumble improvement, by considering a purposely designed masking surface downstream of the intake valve. The main novelty of the paper is, on one hand, the adoption of very high engine compression ratio (CR) values (as explained in the next section), which determine an apparent influence between the induced tumble and the piston. On the other hand, the combined optimization of the cylinder head design and CR, as well as the correlation between numerical and experimental results, represents an added value.

2. PRESENT WORK

The present paper reports part of the outcomes of a research activity carried out by Politecnico di Torino (PoliTo) and Fiat Research Center (CRF) within the Biomethair regional research project (Automotive platform of Regione Piemonte, Italy, http://www.biomethair.it/index.php). The activity has been aimed at giving a contribution to a new urban-mobility solution with ultra-low environmental impact. This ambitious target has been pursued by means of the development and integration of a number of advanced technologies, including hybrid propulsion, high-performance engines as well as biofuel production and utilization.

The activities performed by PoliTo and CRF have been focused on the development of a high-performance engine specifically dedicated to CNG fueling and featuring a variable valve actuation (VVA) system as well as very high compression ratios. The main engine characteristics are reported in Table 1. The engine is derived from the production gasoline-fueled TwinAir engine and the compression ratio (CR) was increased from the baseline value of 10 up to the range 12-14, whose optimization was part of the design process. The results of the Biomethair engine development activity are presented in this paper, as well as in [10]. More precisely, the results of the experimental and numerical characterization of the steady-state tumble flow from the Biomethair engine head were presented in [10]. In addition, a numerical model for the engine-cycle transient simulation was developed and preliminarily assessed. The present paper is focused on the design and optimization activity of the Biomethair combustion chamber. The activity was carried out by combining 3D simulation results to performance and emission data from the dyno test rig at CRF.

Table 1 – Biomethair engine characteristics

Feature	**Value/specification**
Displacement [cm^3]	875
Number of cylinders	2

Compression ratio	12-14 (production engine: 10)
Turbocharger	WG-controlled
Target torque	140 Nm @2000 rpm
Target power	60 kW @5000 rpm

3. ENGINE DEVELOPMENT PROCEDURE

The engine development activity described in the present paper is divided into three parts. First, two variants for the cylinder head geometry were considered and compared, with specific reference to their performance in terms of permeability and tumble intensity. More specifically, the influence of a purposely designed masking surface is analyzed through the comparison with the baseline cylinder head configuration without mask. As a matter of fact, as widely discussed in the Introduction section, the enhancement of the tumble intensity caused by the masking wall can lead to an increase in the turbulence intensity and, in turn, to remarkable benefits in terms of combustion speed, efficiency and repeatability. On the other hand, the presence of an additional obstacle might lead to a detriment in the volumetric efficiency. A steady-state cylinder head numerical model ('virtual flow rig' model), previously developed and validated [10], was applied for this analysis. Second, the selected cylinder head geometry was used to assemble the prototype engine, by considering three different piston variants which corresponded to three different CR values, ranging from 12 to 14. The CR effect was then analyzed by combining experimental and 3D simulation results. Third, the selected compression ratio was finally considered to verify the overall effect of the cylinder head geometry on the in-cylinder tumble, in the presence of combustion.

The baseline versions for the "virtual flow rig" model and the complete engine model adopted in the current study were extensively described and validated in [10], some details are anyhow summarized hereafter for the reader's convenience. The main model features are also summarized in Table 2, along with the associated average calculation time.

Table 2. CFD model summary

	'Virtual flow rig' model	**Engine model**
Cell count	~4,000,000	~800,000 (at BDC)
Cell size	min. 0.3 mm, max. 2.5 mm	min. 0.4 mm, max. 1 mm
Turbulence model	Realizable k-ε	RNG k-ε
Near wall treatment	'Two layer all y+'	Angelberger law of the wall [25]
Combustion model	-	ECFM-3z [26]
Average calculation time	~16h on a 24 CPU workstation	~48h per cycle, on a 24 CPU workstation

The steady-state flow rig model was developed within StarCCM+ v.8.06 and features around 4 million of cells, the mesh size ranging between 1.25-2.5 mm in the intake ports and 0.3 mm in the valve curtain region (Fig. 1a). The Realizable k-ε model turned out to be the best compromise between model accuracy, stability and computational cost, within the Reynolds-Averaged Navier-Stokes (RANS) framework, and was thus selected for the analyses discussed in the present paper. For the near wall treatment, a two-layer

approach named ‘all y+’ was selected and 5 cell layers were placed at the wall boundaries. Such an approach is claimed to provide a reliable solution in the entire y+ range.

The transient engine model has been developed by means of the commercial code Es-ICE version 4.20 and features around 800 000 cells at bottom dead center, with a cell size between 0.4 and 1 mm (Fig. 1b). The RNG k-ε model was adopted, along with the Angelberger law of the wall [25], with a near wall extrusion layer of 0.2 mm, which insures a y+ value ranging between 30 and 100. The three-zone extended coherent flamelet model (ECFM-3z) [26] was used in order to simulate the in-cylinder combustion process. The potential of the model in the engine simulation have been recently further demonstrated in [27,28], with reference to a dual-fuel, partially stratified, SI combustion. In the present work, the model coefficients were calibrated based on experimental data in seven engine working conditions with different engine compression ratios. A maximum error of 3% and 2 deg CA was detected on peak firing pressure and ‘combustion barycenter’ (MFB50) position, respectively. An example of comparison between experimental and CFD data is provided in Fig. 2, where an operation point at 3500 rpm, full load (upper row) and another one at 2000 rpm, bmep=4 bar (lower row) are considered. The calibrated model was applied to the different geometry variants under study by keeping the ECFM coefficients unchanged, thus giving consistency to the analysis.

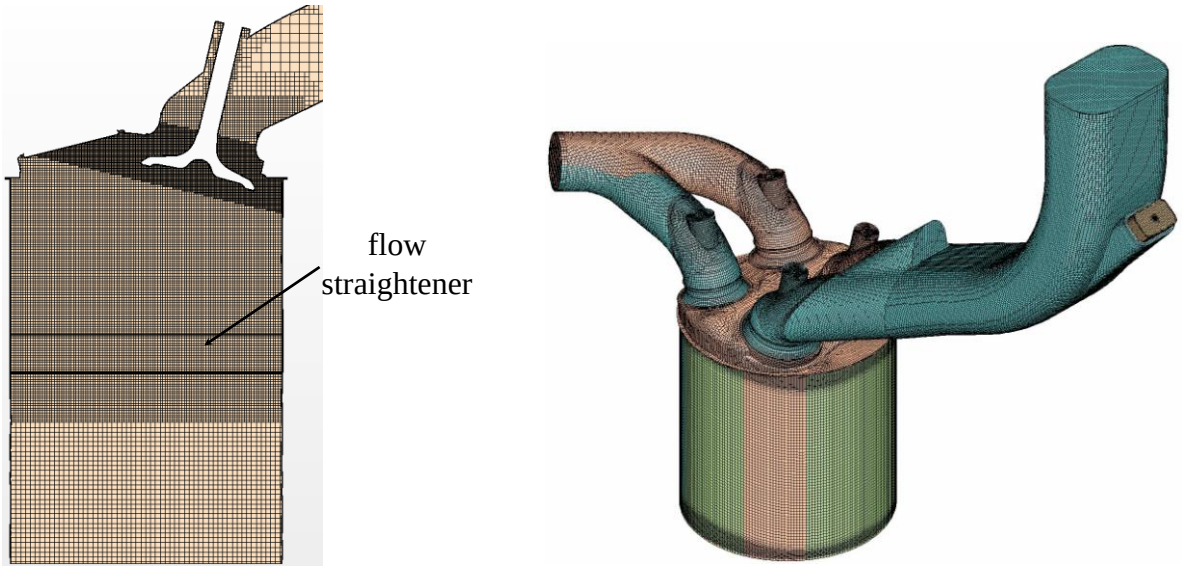

(a) (b)

Figure 1. CFD numerical models: cross- section of the steady-state cylinder head numerical model (‘virtual test rig’) (a); full view of the transient engine model (b).

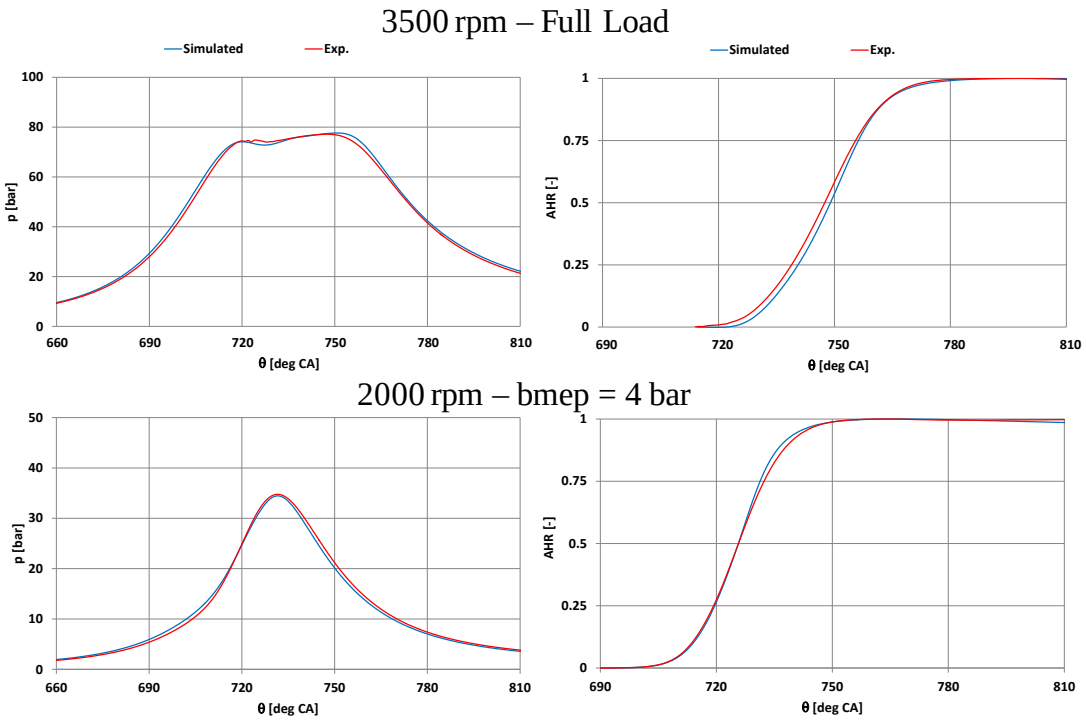

Figure 2. Engine numerical model validation results: pressure (left) and heat release (right) profiles.

4. RESULTS AND DISCUSSION

4.1 Steady-state flow CFD simulation

The first step of the combustion chamber design process was the comparison of two variants for the head dome, which are represented in Fig. 3. In this phase, only the cylinder head is considered, without any piston combined to it, according to the approach of the steady-state cylinder head numerical model (Section 3). The first variant is the baseline one (Fig. 3a), which is adopted in the production gasoline engine. The second variant was obtained by creating a masking wall right downstream of the intake valve, to the wall side, as can be seen in Fig. 3b where the masking wall is highlighted with the red oval. The chamber variants were compared through the simulation of the steady-state flow from the intake valve, by considering the CFD model in Fig. 1a.

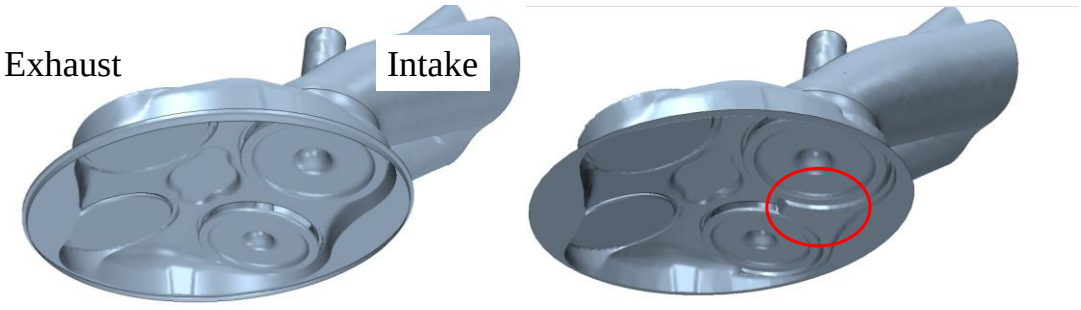

(a) (b)

Figure 3. Design variant: baseline without mask (a) and with mask (b).

The results of the comparison are reported in Figs. 4-6. Fig. 4 shows the steady-state velocity field in the intake valve plane, which was obtained from both variants at the intermediate valve lift of 4 mm. Such a lift value is close to the height of the masking surface in the variant with mask. The figure shows that in the baseline configuration the curtain area of the intake valve is almost entirely exploited and inlet velocities of 100-120 m/s can be observed at both sides of the intake valve (Fig. 4a). The overall tumble intensity thus results from the difference in angular momentum contributions of both the 'direct' and the 'reverse' tumble. Conversely, the 'reverse' tumble is obstructed by the presence of the masking wall in the variant with mask, as it is clearly shown in Fig. 4b. In such a case, the negative contribution due to the flow issuing from the intake valve to the wall side is inhibited to a great extent, thus increasing the overall tumble intensity.

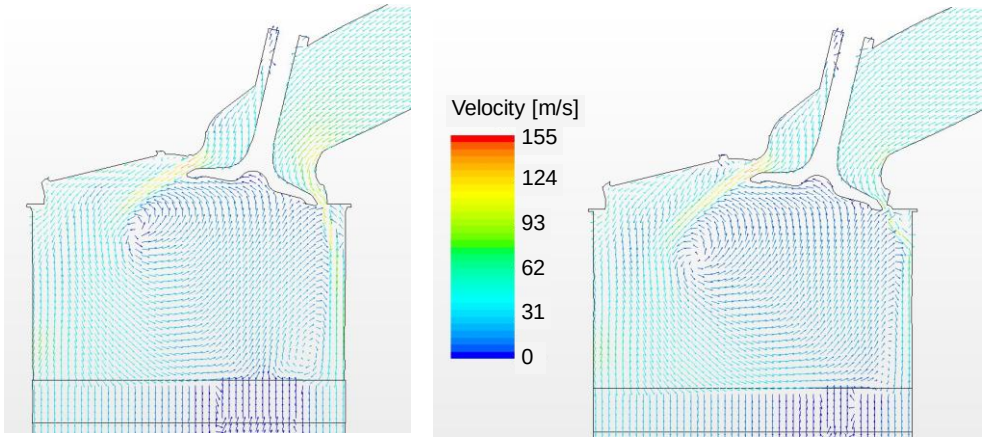

Figure 4. Steady state intake velocity field at the intermediate lift of 4 mm: baseline without mask (a) and with mask (b) configurations.

The effect of the combustion chamber geometry on the valve performance is summarized in Fig. 5 in terms of discharge coefficient and tumble number. The tumble number is given by ([10]):

$$N_T = \frac{-\left(\omega_{av,INT} + \omega_{av,EXH}\right) \cdot B}{v_{is}} \qquad (1)$$

where $\omega_{av,INT}$ and $\omega_{av,EXH}$ are equivalent angular speed referred to the intake and the exhaust side, respectively (see Fig. 3), according to the equation below:

$$\omega_{av,EXH} = \frac{\sum_{e=1}^{N_e} V_{z,e} X_e}{\sum_{e=1}^{N_e} X_e^{\,2}}; \qquad \omega_{av,INT} = \frac{\sum_{i=1}^{N_i} V_{z,i} X_i}{\sum_{i=1}^{N_i} X_i^{\,2}} \tag{2}$$

and v_{is} is the isentropic flow velocity corresponding to the actual pressure ratio. The formulas above are applied with reference to a measurement plane located 2 mm below the flow straightener (Fig. 1a). The position x=0 is the cylinder axis position, and the indices i and e are related to the intake and the exhaust side, respectively. As far as the influence of the chamber design is concerned, for low and intermediate valve lift values the presence of the masking wall gives rise to a decrease of the valve discharge coefficient by around 10-20%, whereas the tumble number is increased up to two-three times its original value, due to the reverse tumble inhibition discussed above. At high lift (above 5 mm), the intake valve results to be displaced beyond the extension of the masking surface, consequently its effect virtually disappears as is testified by the comparable values of both C_D and N_T for the baseline and the 'masked' design.

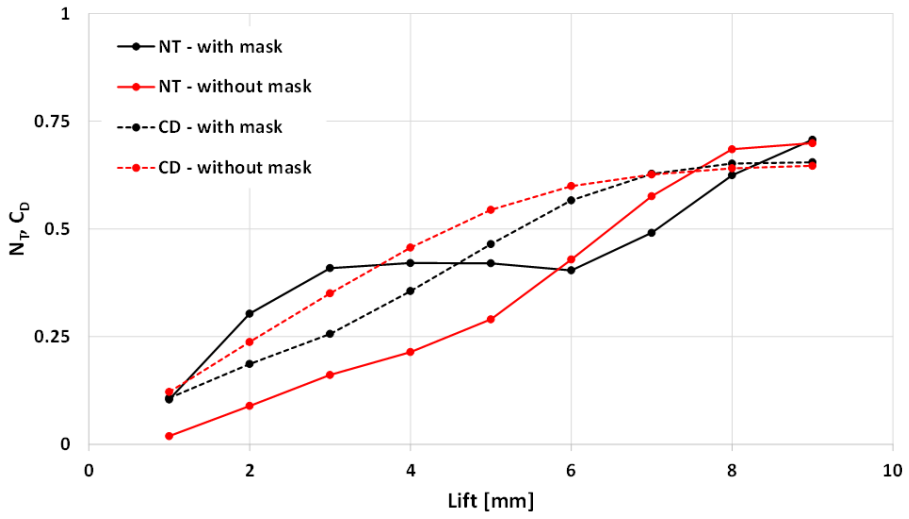

Figure 5. Tumble number (NT) and discharge coefficient (CD) versus valve lift.

The results in Fig. 5 can be used as input to estimate the effect of the mask presence on the global tumble and permeability of the valve in the real engine installation. Following the procedure in [29], with reference to the intake valve lift profile for the considered engine working point, the average discharge coefficient and the steady-state tumble ratio at IVC can be defined as follows:

$$\overline{C_D} = \frac{\int_{\vartheta_1}^{\vartheta_2} C_D \cdot d\vartheta}{\vartheta_2 - \vartheta_1} \tag{3}$$

$$TR = \frac{B \cdot s}{N_v D_v^2} \cdot \frac{\int_{\vartheta_1}^{\vartheta_2} C_D \cdot N_T \cdot d\vartheta}{\left(\int_{\vartheta_1}^{\vartheta_2} C_D \cdot d\vartheta\right)^2} \tag{4}$$

where θ_1 and θ_2 represent the intake valve opening and closure crank angle positions, respectively. The considered coefficients were calculated in three engine working points, as reported in Table 3. The results are reported in Fig. 6. The valve lift profile considered in each of the working points can be found in Fig. 7.

Table 3. Engine working points for tumble ratio evaluation.

Speed [rpm]	bmep [bar]
2000	2
2000	4
3500	Full load

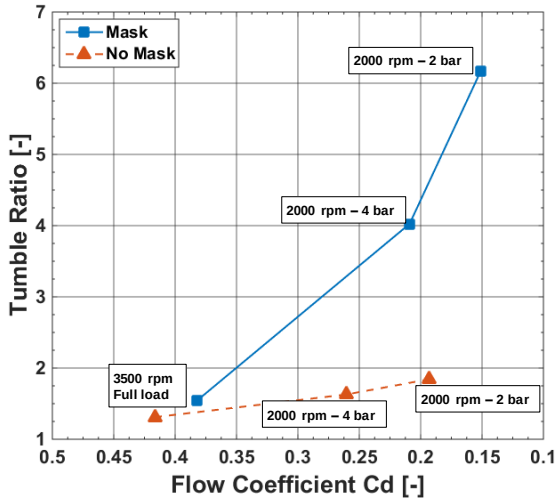

Figure 6. Average flow coefficient and tumble ratio in different engine working points.

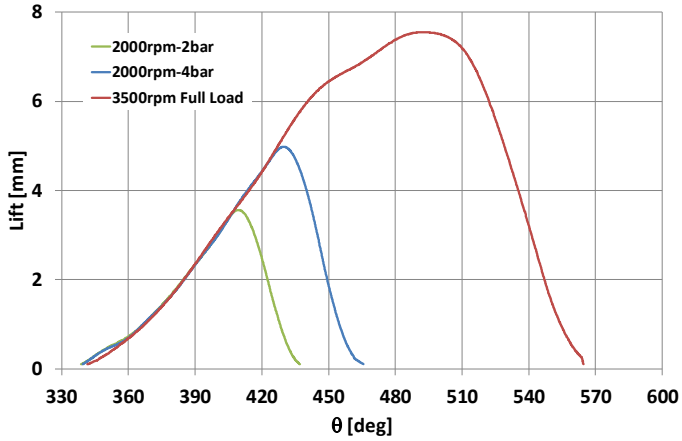

Figure 7. Valve lift profiles.

The results in Fig. 6 show that the presence of the mask determines a decrease in the average discharge coefficient by around 20-30%, mainly due to the reduced effective flow area caused by the obstruction

effect of the wall. As far as the tumble ratio defined by Eq. 4 is concerned, the effect is actually dependent on the engine load. At partial load, the valve opening time and maximum lift are highly reduced by the action of the VVA device (Fig. 7). Consequently, the valve position is kept within the range corresponding to the extension of the masking surface, thus maximizing its effect on the flow unbalance. As a matter of fact, the tumble ratio at partial load is increased by 150% in the 2000rpm-4bar working point, and by 235% in the 2000rpm-2bar one. At full load, the valve lift is kept above 5 mm for about half of the total opening time. It is worth recalling that the mask is virtually ineffective in for high lift, and observing that such lift values affect the integral at the numerator of Eq. 4 to a great extent, due to the high value of C_D in that range. For this reason, the tumble ratio benefit is limited to 18%. Although the tumble ratio estimated by steady-state flow data might not be fully representative of the flow behavior in the real engine [10], their significance is usually sufficient to assess for the suitability of steady flow tests during the early design stages of tumble-generating induction systems [29]. Consequently, based on the results discussed above, it was decided to adopt the configuration with mask for assembling the Biomethair engine prototype, given the minor penalty in the discharge coefficient which accompanies the remarkable tumble increase

4.2 Experimental tests

The experimental results presented in this paper were acquired by CRF and shared with Politecnico di Torino within the Biomethair project. Three values of the compression ratio (namely, 12, 13 and 14) were actually tested, by assembling different piston design variants with the same cylinder head (see Fig. 3). The piston design variants are represented in Fig. 8. The tests aimed at defining the optimal engine CR as a compromise between performance at full load and fuel consumption at partial load.

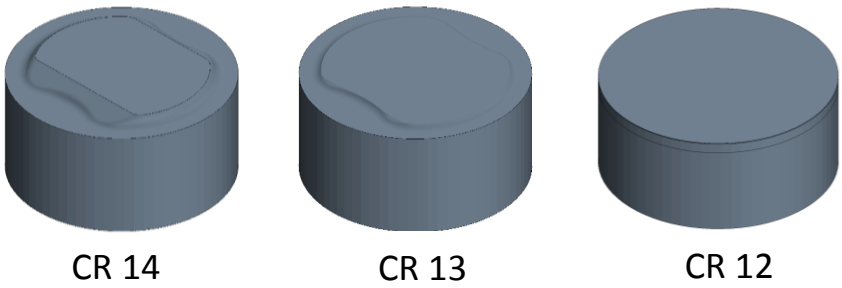

Figure 8. Piston shapes corresponding to the considered compression ratio values.

Figs. 9 and 10 show the results obtained at full load for the three compression ratios. More specifically, Fig. 9 compares the torque and power curves obtained with the three considered CR to the reference curve of the normal production (NP) engine, whereas Fig. 10 reports the CoV of the imep, the ensemble-averaged peak firing pressure (PMAX0) and the maximum cycle resolved peak firing pressure (PMAXmx). In all the cases, the engine calibration was aimed at maximizing the engine load, by taking the compressor surge limit into account. Moreover, the threshold for the ensemble value of the peak firing pressure was set at 85 bar, allowing the single ‘upper’ cycles to reach 100 bar. Such limits led to the limitation of the spark advance (SA) to 5-6 deg CA in most cases. The target performance data were set at 140 Nm and 60 kW. The results showed that the target torque value is achieved with all the CRs. However, the higher one (CR=14) does not

allow the power target to be fulfilled. As far as the cyclic variation of the engine is concerned, an increasing trend of the imep coefficient of variation against CR was found (Fig. 10). This is due to the combination of two effects. First, as CR is increased, the spark timing (ST) had generally to be reduced to keep the peak firing pressure (PFP) within its limit. Second, for a given ST, the increase in CR negatively affects the combustion regularity. This is to be ascribed to the detriment in the tumble intensity evolution during the intake and the compression stroke, as will be shown in Section 4.3, and is evidenced in Fig 11. In the figure, the in-cylinder pressure acquisitions are showed for different CR values in the operating point at 3500 rpm, full load, with the same SA setting. The pressure traces pertaining to individual cycles are represented by light gray lines, whereas the red thick lines show the results of the ensemble average of acquired cycles. The red, dashed line indicates the angular position of the spark timing. As can be seen, the in-cylinder pressure at spark timing increases as CR increases. Moreover, the cycle-resolved pressure traces show a higher dispersion in the CR=14 case, which features both very fast combustion events and misfire cycles. It is thus necessary to further reduce the spark timing in order to reduce the PFP of fast burning cycles. Although the precise control of the limit on the maximum cycle-resolved PFP was rather difficult, and thus the threshold of 100 bar was slightly exceeded in many cases, the obtained results can be considered acceptable as far as the structural integrity of the engine is concerned.

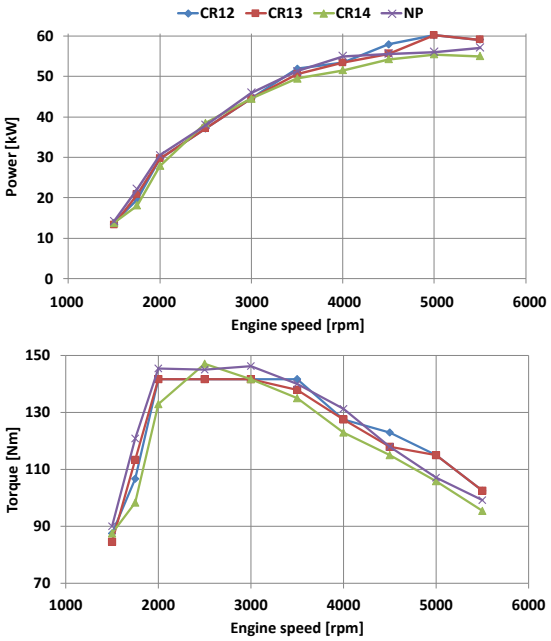

Figure 9. Full load performance curves for the three CR values compared to NP engine.

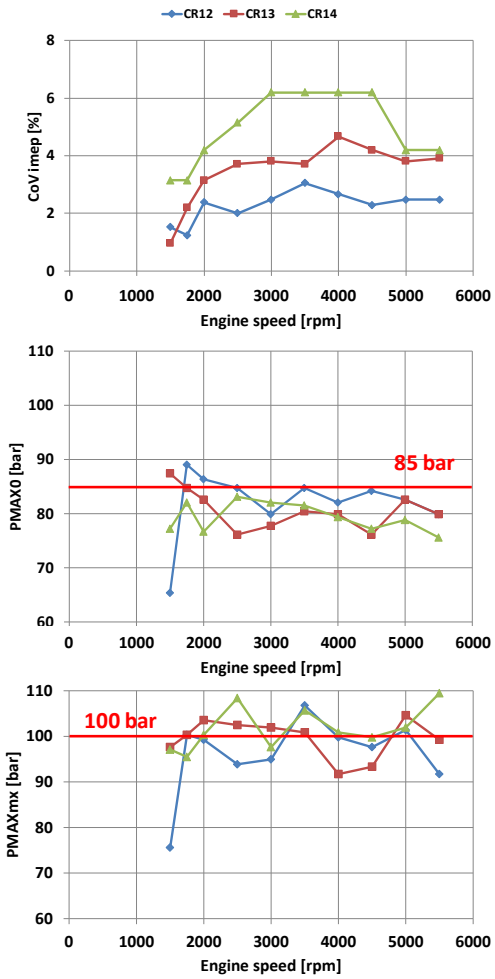

Figure 10. Full load performance curves: CoV imep, average PFP (PMAX0) and maximum cycle-resolved PFP (PMAXmx).

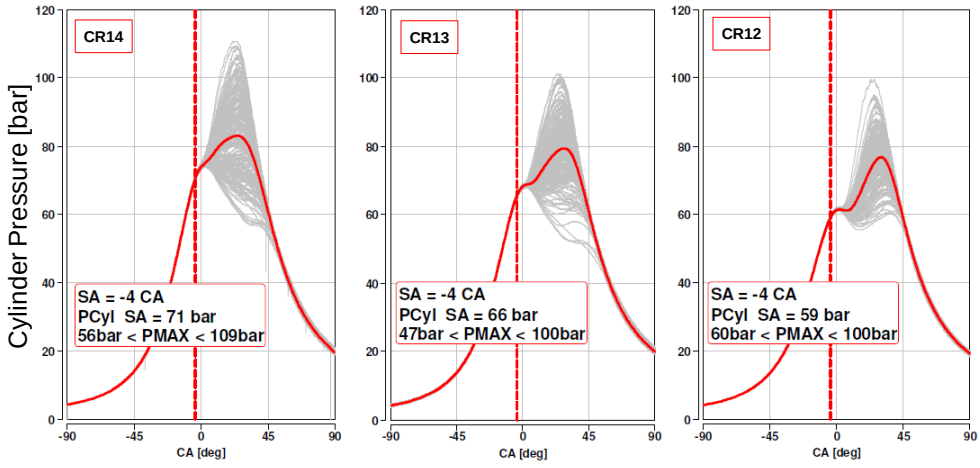

Figure 11. Cycle-by-cycle and average in-cylinder pressure at 3500 rpm, Full load, for CR=14 (left), CR=13 (middle) and CR=12 (right).

The CR effect on engine performance and efficiency was also investigated at partial load. The engine was run in a few selected working points, as detailed in Table 4.

Table 4. Engine working points for experimental tests at partial load.

Speed [rpm]	bmep [bar]
1500	2, 6
2000	2, 3, 4, 6, 8
2500	2, 4, 8, 12
3000	8, 12, 15

The results are presented in Figs. 12 and 13. Fig. 12 shows the engine bsfc reduction, with respect to the base engine with CR=10. As a matter of fact, as CR increases, the efficiency of the reference thermodynamic Otto cycle increases. However, the impact of the thermodynamic losses due to imperfect or untimely combustion process might affect the overall engine behavior. At partial load, no issues about the PFP limit arise, thus the combustion timing can be always set to its optimal value (usually corresponding to MFB50 ranging from 5 to 10 deg after top dead center), corresponding to the maximum brake torque (MBT) conditions. Consequently, the effect of combustion untimeliness is similar for the three CR values, and the dominant effect is given by the increase in the Otto cycle efficiency. Consistently, a benefit in engine fuel consumption was obtained experimentally in almost all the working points at it is shown in Fig. 12. The impact of the engine CR on the combustion cycle-to-cycle variation is represented in Fig. 13 for a few selected engine operating conditions, amongst those included in Table 4. Similarly to the full load case, the combustion process gets less regular as CR increases, again suggesting that a detriment in the turbulence level at combustion start has occurred.

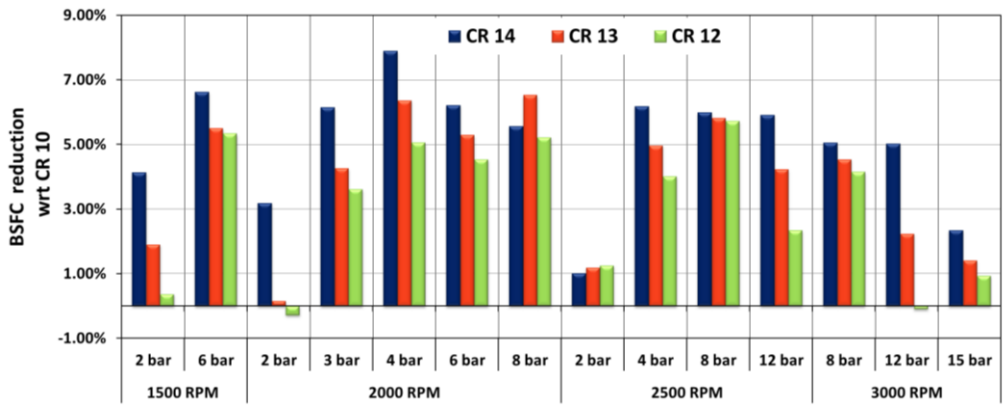

Figure 12. Percentage bsfc reduction with respect to the baseline engine with CR=10, for various working points at MBT timing.

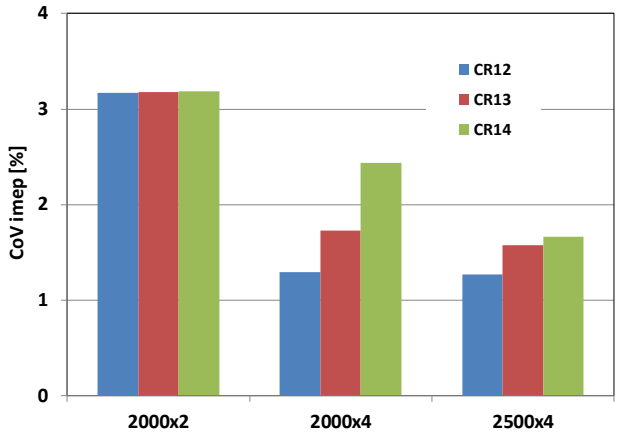

Figure 13. CoV imep in a few selected working points for the different CRs.

The experimental activity carried out by CRF evidenced the following main effects as the compression ratio is increased:

1. The maximum engine power decreases;
2. The bsfc at partial load decreases;
3. The benefit in bsfc at full load are hidden by the non-optimal combustion timing, mainly due to the occurrence of the PFP limitations;
4. The cycle-to-cycle variability of combustion increases both at partial load and at full load.

The CR=13 value was finally selected for equipping the demonstrator vehicle, as the best compromise between fuel consumption at partial load, combustion quality and engine performance at full load.

4.3 Engine transient CFD simulations

A set of CFD simulations was planned aside the experimental activity, focused on investigating the in-cylinder flow and combustion process in the engine cycle. The work was aimed at giving a deeper insight to the combustion behavior in the engine propotype, as well as at verifying the consistency of the steady-state flow simulation results as far as the effect of the masking surface is concerned.

First of all, as a dependence of the combustion speed and cycle-to-cycle variation on the CR was observed, as it is shown in Section 4.2, the engine configuration with mask was simulated with different compression ratio values in order to have an insight into the tumble and turbulence evolution. The results are shown in Figs. 14-15. Fig. 14 reports the in-cylinder velocity field at an intermediate instant of the induction stroke, with reference to the combustion chamber variant with mask. As a matter of fact, for a given crank angle a difference in CR (and, in turn, in the clearance volume) gives rise to a different position of the piston top with respect to the cylinder head. In the CR=14 case, the piston is closer to the head and the intake flow impinges on it, resulting in a decrease in the tumble vortex size and reduction of its overall intensity. Contrariwise, in the lower compression ratio case, the resultant size of the direct tumble structure is bigger and better defined. Fig. 15 shows the tumble number and the mass-averaged turbulence intensity evolution versus crank angle, for the three CR values at 3500 rpm and full load. The in-cylinder tumble number is given by:

$$TN = \frac{\int_{m_{cyl}} \left[-v_z \left(x - x_m \right) + v_x \left(z - z_m \right) \right] \cdot dm_{cyl}}{\frac{2\pi N}{60} \int_{m_{cyl}} \left[\left(x - x_m \right)^2 + \left(z - z_m \right)^2 \right] \cdot dm_{cyl}} \quad (5)$$

where v_x, v_z are the x- and z- components of the velocity, x_m, z_m are the x- and z- coordinates of the cylinder center of mass and N is the engine speed in rpm. As the piston exerts a disturbance effect on the direct tumble vortex throughout the first part of the induction stroke, the TN generation is the higher in the CR=12 case. This happens between around 360 and 450 deg CA, and is the cause of the difference in the TN curves, which can be appreciated in Fig. 15. The higher tumble strength in the case with CR=12 in turn determines a higher turbulence level (by around 20%) in correspondence to the spark timing, hence contributing to the explanation of the observed differences in the combustion speed and stability (Figs. 10, 11 and 13).

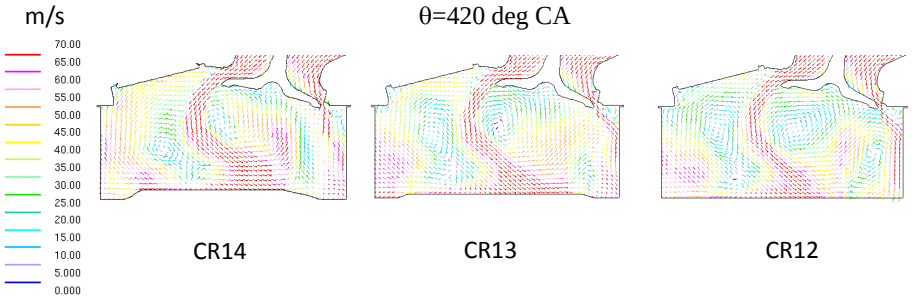

Figure 14. In-cylinder velocity field during the intake stroke for different CR values – 3500 rpm, Full load.

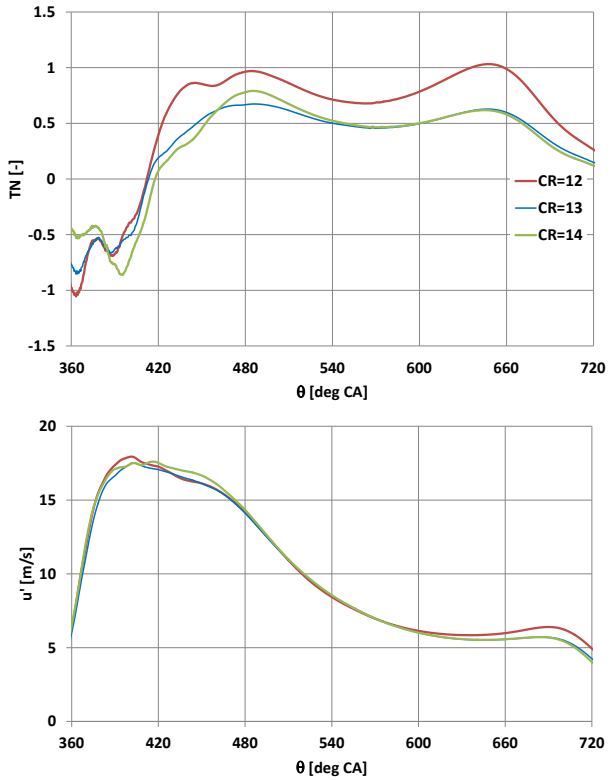

411

412 Figure 15. Tumble number and mass-averaged turbulence intensity versus crank angle – 3500 rpm, Full
413 load.

414

415 Further simulation work was carried out, in order to assess for the differences in fluid-dynamic and
416 turbulence flow features between the baseline configuration and the one with masked intake valve. Fig. 16
417 shows the effect of the combustion chamber variants on the in-cylinder flow field structure at 450 deg CA,
418 for the working point at 2000 rpm and 4 bar, with CR=13. As discussed above, the piston presence affects
419 the overall size of the direct tumble vortex, however the relative effect between the configuration without
420 mask and that with mask is qualitatively the same as the one observed in the steady-state analysis (see Fig.
421 4). In the considered working point, the actuated valve lift profile is represented by the blue line in Fig. 7.
422 Since the maximum lift is kept within the size of the masking wall, the latter is able to exert its influence
423 over the whole intake process. Consequently, a remarkable benefit is obtained in terms of both tumble
424 number and turbulence as can be inferred from Fig. 17. In correspondence to the spark timing position
425 (about 690 deg CA) an increase by around 90% and 10% have been obtained for TN and for the turbulence
426 intensity, respectively, relative to the baseline variant. As far as the full-load conditions are concerned, a
427 considerably lower effect is obtained, due to the higher inlet valve lift. In fact, as discussed in Section 4.1,
428 the masking surface is virtually ineffective when the valve lift is greater than the surface extension. Fig. 18
429 shows an overall evaluation of the mask effect, including full-load as well as partial load cases, for CR=12
430 and CR=13. As can be seen in the figure, with the exception of the full load case with CR=13, the presence
431 of the mask increases the tumble level in the cylinder and, in turn, the turbulence intensity. However, at a
432 first sight a detriment in tumble was also obtained in the 2000 rpm, bmep=2 bar case with CR=12. Still, in
433 such a case the virtually nil TN is actually the result of the compensation of two opposite moment
434 contributions and does not represent a penalty, as it is confirmed by the comparable turbulence level
435 obtained. Concerning the turbulence effect on burning speed, except the CR=13 configuration at full load
436 conditions, a benefit on the combustion duration from 1% to 50% of heat released (MFB1-50) between 2

and 6 deg CA was found. This is in agreement with the observed experimental combustion behavior, also from the point of view of the cycle-to-cycle stability, and confirms the overall benefit that is obtained by adopting the tumble oriented cylinder head design.

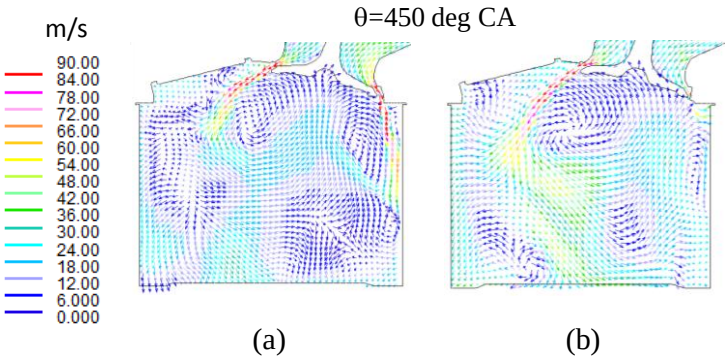

Figure 16. Effect of the intake valve masking surface on in-cylinder flow field at 2000 rpm, bmep=4 bar.

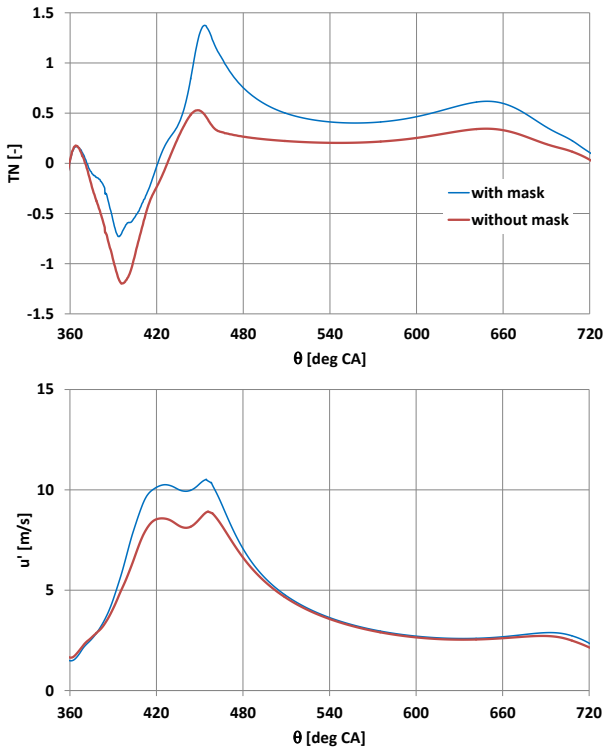

Figure 17. Tumble number and turbulence evolution versus crank angle for the variants with and without mask – 2000 rpm, bmep=4 bar.

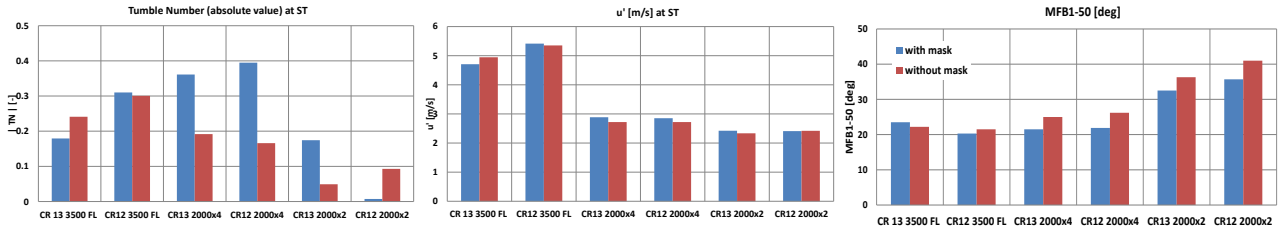

Figure 18. Tumble number, turbulence intensity and MFB1-50 combustion interval for the variants with and without mask.

6. CONCLUSION

The activity presented in this paper was focused on the development of a monofuel, high performance, NG engine. More specifically, the design of the engine combustion chamber was described, with reference to the optimization of the engine CR and to the trade-off between engine permeability and tumble characteristics of the intake port. The activity was carried out by combining 3D simulations and experimental tests. The main conclusions are as follows.

- The steady-state simulations indicated that the engine configuration with mask features a decrease in the average discharge coefficient by around 20-30%, whereas an increase in the tumble ratio by around 200% is obtained at partial load.
- The simulations of the engine cycle led to the same conclusion from a qualitative point of view, though the presence of the piston modifies the tumble intensity of the induced flow with respect to the 'undisturbed' flow in the virtual steady-state flow rig. In the 2000x4 working point, the increase in the tumble number at spark timing was of around 90%, which lead to a 10% increase of the turbulence intensity.
- Overall, the presence of the masking surface determined a benefit in the turbulence intensity at spark timing in almost all the cases at partial load, and a reduction of the MFB1-50 interval between 2 and 6 deg CA was correspondingly obtained.
- With reference to the optimization of the engine CR, the experimental activity carried out at CRF showed that CR=13 was the best compromise between fuel consumption at partial load, engine performance at full load, and combustion quality.
- The cycle-to-cycle variability of combustion increased with the increase in the engine CR, due to the detriment of the tumble number and of the turbulence intensity. The latter is higher by around 20% in the CR=12 case.

7. ACKNOWLEDGEMENTS

Financial support to this activity has been provided within the Biomethair regional research project (Automotive platform of Regione Piemonte, Italy). The authors warmly thank Giorgio Carpegna, Andrea Gerini, Francesco Perna, Andrea Stroppiana of Centro Ricerche Fiat S.C.p.A. for their valuable support.

8. REFERENCES

1. Maclean HL, Lave LB. Evaluating automobile fuel/propulsion system technologies. Prog Energy Combust Sci 2003;29: 1–69.
2. Baratta M, Misul D. Development of a method for the estimation of the behavior of a CNG engine over the NEDC cycle and its application to quantify for the effect of hydrogen addition to methane operations. Fuel 2014; 140: 237-249.
3. Bergthorson JM, Thomson JM. A review of the combustion and emissions properties of advanced transportation biofuels and their impact on existing and future engines. Renewable and Sustainable Energy Reviews 2015 (42): 1393–1417.
4. Cucchiella F, D'Adamo I. Technical and economic analysis of biomethane: A focus on the role of subsidies. Energy Conversion and Management 2016 (119): 338–351.
5. E. Porpatham, A. Ramesh, B. Nagalingam, Investigation on the effect of concentration of methane in biogas when used as a fuel for a spark ignition engine, Fuel, Volume 87, Issues 8–9, July 2008, Pages 1651-1659, ISSN 0016-2361.
6. R. Chandra, V.K. Vijay, P.M.V. Subbarao, T.K. Khura, Performance evaluation of a constant speed IC engine on CNG, methane enriched biogas and biogas, Applied Energy, Volume 88, Issue 11, November 2011, Pages 3969-3977, ISSN 0306-2619.
7. Baratta M, d'Ambrosio S, Misul D, Spessa E. Effects of H2 Addition to CNG Blends on Cycle-To-Cycle and Cylinder-to-Cylinder Combustion Variation in an SI Engine. J. Eng. Gas Turbines Power 136(5), 051502 (Jan 02, 2014) doi:10.1115/1.4026163.
8. Fanhua Ma, Mingyue Wang, Long Jiang, Jiao Deng, Renzhe Chen, Nashay Naeve, Shuli Zhao, Performance and emission characteristics of a turbocharged spark-ignition hydrogen-enriched compressed natural gas engine under wide open throttle operating conditions, International Journal of Hydrogen Energy, Volume 35, Issue 22, November 2010, Pages 12502-12509, ISSN 0360-3199.
9. Amer AA, Reddy TN. Multidimensional Optimization of In-Cylinder Tumble Motion for the New Chrysler Hemi. SAE Tech Paper 2002-01-1732, 2002.
10. Baratta M, Misul D, Spessa E, et al. Experimental and numerical approaches for the quantification of tumble intensity in high-performance SI engines. Energy Conversion and Management 138, pp. 435–451, 2017. http://dx.doi.org/10.1016/j.enconman.2017.02.018.
11. Berntsson A, Josefsson G, Ekdahl R, Ogink R, et al. The Effect of Tumble Flow on Efficiency for a Direct Injected Turbocharged Downsized Gasoline Engine. SAE Int. J. Engines 4(2):2298-2311, 2011. https://doi.org/10.4271/2011-24-0054.
12. Saito H, Shirasuna T, Nomura T. Extension of Lean Burn Range by Intake Valve Offset. SAE Int. J. Engines 6(4):2072-2084, 2013. https://doi.org/10.4271/2013-32-9032.
13. Zhou F, Fu J, Ke W, et al. Effects of lean combustion coupling with intake tumble on economy and emission performance of gasoline engine. Energy 133:366-379, 2017.
14. Zhang Z, Zhang H, Wang T, et al. Effects of tumble combined with EGR (exhaust gas recirculation) on the combustion and emissions in a spark ignition engine at part loads, Energy 65, 1: 18-24, 2014.
15. Fu J, Zhu G, Zhou F, et al. Experimental investigation on the influences of exhaust gas recirculation coupling with intake tumble on gasoline engine economy and emission performance. Energy Conversion and Management 127 (2016): 424-436.
16. Ogink R, Babajimopoulos A. Investigating the Limits of Charge Motion and Combustion Duration in a High-Tumble Spark-Ignited Direct-Injection Engine. SAE Int. J. Engines 9(4):2129-2141, 2016. https://doi.org/10.4271/2016-01-2245.

17. Fu J, Zhu G, Zhou F, et al. Experimental investigation on the influences of exhaust gas recirculation coupling with intake tumble on gasoline engine economy and emission performance. Energy Conversion and Management 127: 424–436, 2016.
18. Yang J, Dong X, Wu Q, Xu M. Effects of enhanced tumble ratios on the in-cylinder performance of a gasoline direct injection optical engine. Applied Energy 236: 137–146, 2019.
19. Iyer C, and Yi J. 3D CFD Upfront Optimization of the In-Cylinder Flow of the 3.5L V6 EcoBoost Engine. SAE Tech Paper 2009-01-1492, 2009. https://doi.org/10.4271/2009-01-1492.
20. Takahashi D, Nakata K, Yoshihara Y, Omura T. Combustion Development to Realize High Thermal Efficiency Engines," SAE Int. J. Engines 9(3):2016. doi:10.4271/2016-01-0693.
21. Sun Y, Wang T, Lu Z, et al. The Optimization of Intake Port using Genetic Algorithm and Artificial Neural Network for Gasoline Engines. SAE Tech Paper 2015-01-1353, 2015. doi:10.4271/2015-01-1353.
22. Abidin Z, Hoag K, Mckee D, Badain N. Port Design for Charge Motion Improvement within the Cylinder. SAE Tech Paper 2016-01-0600, 2016. https://doi.org/10.4271/2016-01-0600.
23. Millo F, Luisi S, Borean F, Stroppiana A. Numerical and experimental investigation on combustion characteristics of a spark ignition engine with an early intake valve closing load control. Fuel 121:298-310, 2014.
24. Sagaya Raj A, Maharudrappa Mallikarjuna J, Ganesan V. Energy efficient piston configuration for effective air motion – A CFD study. Applied Energy 102: 347-354, 2013.
25. Angelberger C, Poinsot T, Delhay, B. Improving near-wall combustion and wall heat transfer modeling in SI engine computations. SAE Tech Paper 972881; 1997.
26. Colin O, Benkenida A. The 3-Zones Extended Coherent Flame Model (ECFM-3z) for Computing Premixed/Diffusion Combustion. Oil & Gas Science and Technology - Rev. IFP 59 (6) 593-609, 2004.
27. Huang Y, Hong G, Huang R. Numerical investigation to the dual-fuel spray combustion process in an ethanol direct injection plus gasoline port injection (EDI + GPI) engine. Energy Conversion and Management 92: 275–286, 2015.
28. Huang Y, Hong G, Huang R. Effect of injection timing on mixture formation and combustion in an ethanol direct injection plus gasoline port injection (EDI+GPI) engine. Energy 111: 92-103, 2016.
29. Arcoumanis C, Hu Z, Whitelaw JH. Steady flow characterization of tumble-generating four-valve cylinder heads. Proc of Instit Mech Eng, Part D: J of Automobile Eng 207: 203-210, 1993.